The Astrophysical Journal, 932:66 (16pp), 2022 June 10 https://doi.org/10.3847/1538-4357/ac6dd7

Insight-HXMT Study of the Inner Accretion Disk in the Black Hole Candidate EXO 1846–031

X. Q. Ren[1,2], Yanan Wang[3], S. N. Zhang[1], R. Soria[4,5], L. Tao[1], L. Ji[6], Y. J. Yang[7,8], J. L. Qu[1], S. Zhang[1], L. M. Song[1], M. Y. Ge[1], Y. Huang[1], X. B. Li[1], J. Y. Liao[1], H. X. Liu[1,2], R. C. Ma[1,2], Y. L. Tuo[1], P. J. Wang[1,2], W. Zhang[1,2], and D. K. Zhou[1,2]

[1] Key Laboratory of Particle Astrophysics, Institute of High Energy Physics, Chinese Academy of Sciences, Beijing 100049, People's Republic of China zhangsn@ihep.ac.cn
[2] University of Chinese Academy of Sciences, Chinese Academy of Sciences, Beijing 100049, People's Republic of China
[3] Physics & Astronomy, University of Southampton, Southampton, Hampshire SO17 1BJ, UK; Y.Wang@soton.ac.uk
[4] College of Astronomy and Space Sciences, University of the Chinese Academy of Sciences, Beijing 100049, People's Republic of China
[5] Sydney Institute for Astronomy, School of Physics A28, The University of Sydney, Sydney, NSW 2006, Australia
[6] School of Physics & Astronomy, Sun Yat-Sen University, Zhuhai 519082, People's Republic of China
[7] Department of Physics, The University of Hong Kong, Pokfulam Road, Hong Kong
[8] Laboratory for Space Research, The University of Hong Kong, Hong Kong
Received 2021 September 29; revised 2022 April 15; accepted 2022 May 5; published 2022 June 16

Abstract

We study the spectral evolution of the black hole candidate EXO 1846−031 during its 2019 outburst, in the 1–150 keV band, with the Hard X-ray Modulation Telescope. The continuum spectrum is well modeled with an absorbed disk-blackbody plus cutoff power law, in the hard, intermediate, and soft states. In addition, we detect an ≈6.6 keV Fe emission line in the hard intermediate state. Throughout the soft intermediate and soft states, the fitted inner disk radius remains almost constant; we suggest that it has settled at the innermost stable circular orbit (ISCO). However, in the hard and hard intermediate states, the apparent inner radius was unphysically small (smaller than the ISCO), even after accounting for the Compton scattering of some of the disk photons by the corona in the fit. We argue that this is the result of a high hardening factor, $f_{\rm col} \approx 2.0$–2.7, in the early phases of the outburst evolution, well above the canonical value of 1.7 suitable for a steady disk. We suggest that the inner disk radius was already close to the ISCO in the low/hard state. Furthermore, we propose that this high value of the hardening factor in the relatively hard state was probably caused by the additional illuminating of the coronal irradiation onto the disk. Additionally, we estimate the spin parameter using the continuum-fitting method, over a range of plausible black hole masses and distances. We compare our results with the spin measured using the reflection-fitting method and find that the inconsistency of the two results is partly caused by different choices of $f_{\rm col}$.

Unified Astronomy Thesaurus concepts: Black hole physics (159); High energy astrophysics (739); Accretion (14)

Supporting material: machine-readable tables

1. Introduction

A black hole (BH) low-mass X-ray binary is composed of a stellar-mass BH and a companion star with a mass similar to or lower than the solar mass. Such a system normally experiences a long period of quiescence, followed by a short-lived outburst lasting for months to years (Tanaka & Shibazaki 1996; Chen et al. 1997; Tomsick & Kaaret 2000). During an outburst, its luminosity varies by several orders of magnitude (Remillard & McClintock 2006; Reynolds & Miller 2013; Plotkin et al. 2015; Aneesha et al. 2019). The variability is usually detected on timescales as short as milliseconds (van der Klis 2006; Belloni & Stella 2014; Motta 2016). In addition, complex spectral features (Remillard & McClintock 2006; Tao et al. 2018) are also seen during outbursts.

A typical outburst is usually divided into several different spectral states (Fender et al. 2004; Homan & Belloni 2005; Done et al. 2007), based on their spectral and timing behavior. In the initial phase of the outburst (the low hard state, or LHS), the luminosity is low and the spectrum is dominated by a nonthermal hard component with a power-law form. In the standard scenario, the accretion disk is truncated far from the innermost stable circular orbit (ISCO; Esin et al. 1997), and the inner region is filled with a hot, geometrically thick, radiatively inefficient flow (Narayan & Yi 1995). In an alternative scenario, a relatively cool inner disk (in addition to a hot corona and an outer, truncated disk) may also exist near the ISCO (Miller et al. 2006; Liu et al. 2007). Radio observations in the LHS show the presence of a compact jet launched from the innermost region (Fender et al. 2004). At this stage, strong noise components dominate the power density spectra and a low-frequency quasiperiodic oscillation (LFQPO) starts to show up (Remillard & McClintock 2006). As the accretion rate increases, the source enters the hard intermediate state (HIMS) and the soft intermediate state (SIMS), and the spectrum gradually softens. The compact jet disappears between the HIMS and the SIMS. As the accretion rate increases further, the source enters the high soft state (HSS) and the accretion disk reaches the ISCO (or, in the alternative scenario, the outer disk joins the inner disk, removing the coronal gap). In the HSS, the X-ray spectrum is dominated by the disk component (Mitsuda et al. 1984; Makishima et al. 1986). LFQPOs nearly disappear at this stage, although occasionally there are some faint

signs of oscillations (Motta et al. 2012; Belloni & Motta 2016). Later on, the source decays in flux, and passes through the lower-intensity intermediate and hard states, before returning back to quiescence. For a canonical BH transient, the evolution of a full outburst presents a counterclockwise q-shaped loop on the hardness–intensity diagram (Homan et al. 2001; Belloni et al. 2005; Zhang et al. 2020a).

Studying the intrinsic properties of an accretion disk (e.g., the disk temperature and inner disk radius) helps us to better understand the physical phenomena that occur during an outburst; however, this inference relies on an accurate measurement of the disk emission. The observed disk spectrum must be corrected for the fraction of emitted disk photons that have been upscattered into the power-law component (Shimura & Takahara 1995; Peris et al. 2016). To do so, Steiner et al. (2009) developed a self-consistent disk-corona model, named `simpl`, which accounts for the fraction of Compton-scattered disk photons in the computation of the total disk emission (Yao et al. 2005). This model provides a more accurate normalization of the disk emission, and therefore of the apparent inner disk radius and color temperature (Steiner et al. 2017; Sridhar et al. 2020; Zdziarski et al. 2021). The true physical radius and effective temperature are then related to the apparent (fitted) radius and temperature via a hardening factor $f_{\rm col}$ (Kubota et al. 1998). Numerical simulations (Shimura & Takahara 1995; Davis et al. 2005; Shafee et al. 2006) suggest a canonical value of $f_{\rm col}$ ~1.6–1.8. However, some studies suggest that the value of $f_{\rm col}$ varies during the outburst evolution (e.g., Merloni et al. 2000; Davis & El-Abd 2019; Guan et al. 2021), especially in the LHS and the HIMS (e.g., Dunn et al. 2011; Salvesen et al. 2013).

The accurate estimation of the disk emission is also important for the measurement of the spin parameter, especially for the continuum-fitting method (Zhang et al. 1997b; McClintock et al. 2014). The other main technique for measuring the spin parameter is the reflection-fitting method (Fabian et al. 1989; Reynolds 2014). However, the results obtained from the two techniques do not always agree with each other when the spin is nonextremal, i.e., $a_* < 0.9$ (Miller et al. 2009; Steiner et al. 2011). Salvesen & Miller (2021) found that the discrepancies on the spin measurements can be brought into agreement when we account for the uncertainties on $f_{\rm col}$.

To constrain the disk parameters, the coronal parameters, and the hardening factor over the outburst evolution, broadband X-ray spectral coverage is required, so that the thermal component and the Comptonized component can be fitted simultaneously and self-consistently. This is why our team has been monitoring BH outbursts with the Hard X-ray Modulation Telescope (Insight-HXMT), over the ≈1–150 keV band. One of the X-ray transients that we have studied (the subject of this work) is EXO 1846–031, located at R.A. $= 18^{\rm h}49^{\rm m}16\overset{\rm s}{.}99$, decl. $= -03°03'55\overset{''}{.}4$, with a 90% error radius of ≈2″ (Mereminskiy et al. 2019).

The first outburst of EXO 1846–031 was detected by EXOSAT on 1985 April 3 (Parmar et al. 1993), and lasted for several months. After that, the source stayed in hibernation for over 30 yr. Based on its spectrum being associated with an ultrasoft component and a hard power-law tail, Parmar et al. (1993) suggested EXO 1846–031 to be a BH candidate. The recent outburst was first reported by MAXI/GSC (Negoro et al. 2019) on 2019 July 23. The outburst was followed in the radio bands with the Very Large Array (VLA; Miller-Jones et al. 2019) and MeerKAT (Williams et al. 2019), and in the X-ray bands with NuSTAR (Miller et al. 2019), NICER (Bult et al. 2019), and Swift. Insight-HXMT was also triggered by Target of Opportunity (ToO) observations (Yang et al. 2019a, 2019b) of the source from 2019 August 2 to October 25. Draghis et al. (2020) found an obvious reflection feature in the NuSTAR spectrum. They reported an inclination angle of $(73 \pm 1)°$ of the accretion disk and a high spin value of $0.997^{+0.001}_{-0.002}$. Wang et al. (2021) investigated the spectral properties in the HIMS and the HSS with NuSTAR and Insight-HXMT, respectively. They suggested that the reflection component observed in the two spectral states originates from different sources of illumination; they also found that the disk wind and the jet probably co-existed in the HIMS in this source. Liu et al. (2021) performed a detailed timing analysis with the observations of Insight-HXMT, NICER, and MAXI, and found LFQPOs in the HIMS.

In this paper, we report on the broadband spectral evolution of EXO 1846–031 using the Insight-HXMT observations. In particular, we will show the effect of Compton scattering and a variable hardening factor on our measurement of the disk parameters. Additionally, we measure the spin parameter with the continuum-fitting method and compare it with the one derived from the reflection-fitting method. The paper is organized as follows. In Section 2, we introduce the observations and data processing methods. The results are presented in Section 3. The discussion and conclusion follow in Sections 4 and 5, respectively.

2. Observations and Data Reduction

2.1. Observations

Following the MAXI/GSC discovery of a new outburst of EXO 1846–031, we triggered Insight-HXMT ToO observations, which covered 85 days, from 2019 August 2 to October 25 (Table 1).

Insight-HXMT (Zhang et al. 2014, 2020b) is the first Chinese X-ray astronomy satellite, launched on 2017 June 15. It has a 550 km low-Earth orbit, with an inclination of 43°. It contains three slat-collimated instruments, sensitive to different energy ranges: the High Energy (HE; Liu et al. 2020), Medium Energy (ME; Cao et al. 2020), and Low Energy (LE; Chen et al. 2020) X-ray Telescopes. HE, ME, and LE are sensitive to the 20.0–250.0 keV, 5.0–30.0 keV, and 1.0–15.0 keV bands, with detection areas of 5100 $\rm cm^2$, 952 $\rm cm^2$, and 384 $\rm cm^2$, respectively. The corresponding time resolutions are 4 μs, 240 μs, and 1 ms.

2.2. Data Reduction

We used the Insight-HXMT Data Analysis software (HXMTDAS) v2.02[9] to analyze all the data. The filtering criteria for the good time intervals were: (1) an offset angle from the pointing direction $<0\overset{\circ}{.}04$; (2) a pointing direction above earth $>10°$; (3) a value of the geomagnetic cutoff rigidity >8 GeV; and (4) a rejection of data within 300 s of the South Atlantic Anomaly passage. A detailed explanation of the Insight-HXMT data reduction is published on its website.[10] The background rates were estimated with the tools *lebkgmap*, *mebkgmap*, and *hebkgmap* (version 2.0.9), based on the standard Insight-HXMT background models (Liao et al. 2020a, 2020b;

[9] http://hxmt.org/software.jhtml
[10] http://hxmt.org/SoftDoc.jhtml

Table 1
Insight-HXMT Observations of EXO 1846–031

ExpID[a]	Start Time (day)	Start Time (MJD)	HE Rate[b] (cts s^{-1})	ME Rate[c] (cts s^{-1})	LE Rate[d] (cts s^{-1})	HE Exp[e] (s)	ME Exp (s)	LE Exp (s)	State
0101	2019-08-02T06:14:48	58697.35	263.6 ± 0.3	51.58 ± 0.15	67.8 ± 0.3	3001	2359	718	LHS
0102	2019-08-02T10:09:02	58697.50	245.2 ± 0.3	51.0 ± 0.2	71.5 ± 0.2	3062	1964	1436	LHS
0103	2019-08-02T13:19:55	58697.63	241.2 ± 0.3	51.7 ± 0.2	72.1 ± 0.3	2816	1823	762	LHS
0104	2019-08-02T16:30:48	58697.78	233.1 ± 0.3	50.8 ± 0.2	74.1 ± 0.3	1987	1703	718	LHS
0105	2019-08-02T19:41:41	58697.95	229.0 ± 0.6	49.9 ± 0.2	75.5 ± 0.2	616	1637	1715	LHS
0106	2019-08-02T22:52:33	58698.03	215.2 ± 0.3	50.0 ± 0.2	78.5 ± 0.4	2896	1890	563	LHS
0107	2019-08-03T02:03:26	58698.18	200.2 ± 0.4	49.8 ± 0.5	80.3 ± 0.4	447	1350	656	LHS
0201	2019-08-04T07:33:08	58699.40	182.1 ± 0.2	50.43 ± 0.14	103.7 ± 0.4	3892	2751	690	LHS
0301	2019-08-05T07:24:32	58700.39	163.0 ± 0.2	48.97 ± 0.14	123.4 ± 0.4	3643	2540	700	HIMS
0302	2019-08-05T11:18:58	58700.55	158.8 ± 0.2	48.8 ± 0.2	123.1 ± 0.3	2548	1500	1102	HIMS
0303	2019-08-05T14:29:49	58700.66	147.4 ± 0.3	47.2 ± 0.2	132.1 ± 0.7	1421	848	299	HIMS
0401	2019-08-06T02:29:39	58701.26	179.3 ± 0.6	49.6 ± 0.4	127.1 ± 0.7	500	287	299	HIMS
0502	2019-08-07T05:47:50	58702.32	158.1 ± 0.2	47.1 ± 0.2	139.3 ± 0.4	2768	1880	691	HIMS
0503	2019-08-07T09:26:08	58702.45	156.5 ± 0.4	47.4 ± 0.2	134.3 ± 0.5	1255	794	539	HIMS
0601	2019-08-08T02:12:29	58703.21	150.0 ± 0.4	47.1 ± 0.2	153.0 ± 0.4	768	1311	1130	HIMS
0701	2019-08-08T21:17:40	58703.94	129.9 ± 0.2	42.4 ± 0.2	199.4 ± 0.4	2549	1564	1163	HIMS
0703	2019-08-09T03:48:43	58704.20	138.5 ± 0.3	43.6 ± 0.2	178.9 ± 0.5	1659	1314	838	HIMS
0801	2019-08-10T06:41:48	58705.36	106.4 ± 0.2	32.94 ± 0.12	178.3 ± 0.3	1883	2147	1592	HIMS
0802	2019-08-10T10:35:08	58705.53	109.2 ± 0.2	35.64 ± 0.14	220.5 ± 0.4	2742	1864	1371	HIMS
0803	2019-08-10T13:45:57	58705.63	134.4 ± 0.4	35.5 ± 0.2	208.7 ± 0.6	814	959	658	HIMS
0901	2019-08-13T01:30:34	58708.17	109.8 ± 0.2	33.3 ± 0.2	166.8 ± 0.4	1836	1266	835	HIMS
0902	2019-08-13T05:22:20	58708.30	112.4 ± 0.2	35.08 ± 0.15	153.9 ± 0.4	2421	1631	1197	HIMS
1001	2019-08-16T12:15:31	58711.55	91.6 ± 0.3	30.6 ± 0.1	125.0 ± 0.2	1164	2994	2765	HIMS
1002	2019-08-16T16:03:46	58711.75	91.5 ± 0.2	30.95 ± 0.13	119.3 ± 0.3	2247	1777	1736	HIMS
1003	2019-08-16T19:14:36	58711.85	98.1 ± 0.4	31.0 ± 0.2	118.4 ± 0.4	696	671	599	HIMS
1101	2019-08-18T07:14:35	58713.38	75.8 ± 0.2	23.1 ± 0.1	147.3 ± 0.3	3342	2324	2072	HIMS
1102	2019-08-18T11:00:05	58713.50	66.8 ± 0.2	23.7 ± 0.1	153.9 ± 0.3	1538	2202	1975	HIMS
1103	2019-08-18T14:10:56	58713.70	62.7 ± 0.5	23.65 ± 0.14	153.8 ± 0.4	264	1255	1229	HIMS
1301	2019-08-22T06:47:11	58717.38	26.9 ± 0.1	7.84 ± 0.06	115.2 ± 0.3	2714	1867	1399	SIMS
1303	2019-08-22T13:36:56	58717.68	20.6 ± 0.1	7.24 ± 0.11	113.6 ± 0.4	917	589	599	SIMS
1501	2019-08-27T18:51:16	58722.88	35.0 ± 0.1	7.26 ± 0.05	105.5 ± 0.2	3534	3039	2119	SIMS
1601	2019-08-28T21:53:27	58723.99	33.79 ± 0.08	9.16 ± 0.05	121.7 ± 0.3	4836	3419	1541	SIMS
1701	2019-09-03T01:55:34	58729.16	20.7 ± 0.1	6.18 ± 0.07	165.0 ± 1.0	2048	1370	397	SIMS
1702	2019-09-03T05:25:45	58729.31	27.6 ± 0.2	5.30 ± 0.05	165.7 ± 0.4	556	2391	1257	SIMS
1703	2019-09-03T08:44:47	58729.44	32.4 ± 0.1	7.19 ± 0.05	168.7 ± 0.4	3297	2398	1217	SIMS
1801	2019-09-05T12:45:46	58731.63	26.04 ± 0.12	8.01 ± 0.04	187.4 ± 0.3	1901	3967	1533	SIMS
1901	2019-09-07T17:14:33	58733.82	28.45 ± 0.08	8.27 ± 0.06	196.3 ± 0.3	3952	2610	2040	HSS
2201	2019-09-15T01:49:09	58741.21	6.98 ± 0.06	3.56 ± 0.04	189.3 ± 0.5	1666	1839	718	HSS
2202	2019-09-15T05:20:18	58741.31	6.80 ± 0.04	3.68 ± 0.04	186.4 ± 0.4	3896	2486	1436	HSS
2204	2019-09-15T11:52:26	58741.57	4.30 ± 0.04	3.09 ± 0.04	180.0 ± 0.3	2889	1967	2179	HSS
2205	2019-09-15T15:03:15	58741.70	1.37 ± 0.02	3.62 ± 0.04	180.1 ± 0.3	2876	1920	2155	HSS
2206	2019-09-15T18:14:04	58741.84	9.43 ± 0.07	4.82 ± 0.06	183.4 ± 0.4	2037	1348	1162	HSS
2208	2019-09-16T00:35:41	58742.10	15.5 ± 0.2	3.20 ± 0.06	179.6 ± 0.5	480	1047	838	HSS
2209	2019-09-16T03:46:30	58742.24	9.65 ± 0.05	3.46 ± 0.04	180.9 ± 0.5	3889	2584	838	HSS
2210	2019-09-16T06:52:15	58742.33	10.88 ± 0.08	3.49 ± 0.04	181.8 ± 0.4	1752	2313	958	HSS
2211	2019-09-16T10:08:08	58742.53	12.63 ± 0.09	3.87 ± 0.04	179.0 ± 0.3	1437	2046	1482	HSS
2212	2019-09-16T13:18:57	58742.63	7.18 ± 0.05	3.25 ± 0.04	178.0 ± 0.3	2928	1977	2274	HSS
2213	2019-09-16T16:29:46	58742.76	10.70 ± 0.06	4.23 ± 0.05	180.6 ± 0.3	2645	1785	1556	HSS
2214	2019-09-16T19:40:35	58742.89	1.51 ± 0.05	3.52 ± 0.08	179.7 ± 0.7	824	555	359	HSS
2215	2019-09-16T22:51:24	58743.03	31.4 ± 0.3	5.76 ± 0.12	193.4 ± 0.6	286	387	619	HSS
2301	2019-09-19T14:02:31	58745.71	20.40 ± 0.07	7.91 ± 0.06	181.3 ± 0.3	3672	2490	2693	HSS
2401	2019-09-21T04:14:14	58747.21	28.32 ± 0.12	8.06 ± 0.05	172.1 ± 0.2	1873	3466	2858	HSS
2601	2019-09-23T02:23:00	58749.19	6.18 ± 0.04	2.32 ± 0.03	159.8 ± 0.3	3664	3677	2274	HSS
2701	2019-09-25T00:31:11	58751.14	20.13 ± 0.07	4.30 ± 0.03	160.8 ± 0.3	4617	3725	1855	HSS
2801	2019-09-26T00:22:50	58752.13	11.91 ± 0.06	3.07 ± 0.03	152.3 ± 0.3	3701	3639	1556	HSS
2901	2019-09-27T09:46:58	58753.51	4.60 ± 0.03	1.80 ± 0.02	140.6 ± 0.3	4988	3443	1377	HSS
3001	2019-09-29T22:13:09	58756.03	6.34 ± 0.04	1.95 ± 0.02	136.1 ± 0.3	4537	3129	1317	HSS
3102	2019-10-01T04:34:57	58757.28	8.58 ± 0.05	1.63 ± 0.03	127.9 ± 0.4	2925	1884	761	HSS
3103	2019-10-01T08:01:33	58757.40	7.68 ± 0.05	2.08 ± 0.03	128.4 ± 0.5	2768	1874	479	HSS
3203	2019-10-03T07:45:33	58759.39	3.66 ± 0.04	1.38 ± 0.03	125.1 ± 0.8	2531	1726	898	HSS
3301	2019-10-05T05:26:59	58761.30	18.64 ± 0.07	3.70 ± 0.04	122.0 ± 0.3	4398	2966	1736	HSS
3302	2019-10-05T09:04:46	58761.46	11.38 ± 0.06	3.39 ± 0.04	119.5 ± 0.6	3211	2074	388	HSS
3303	2019-10-05T12:15:40	58761.56	24.76 ± 0.15	5.03 ± 0.08	120.3 ± 0.7	1143	712	239	HSS

Table 1
(Continued)

ExpID[a]	Start Time (day)	Start Time (MJD)	HE Rate[b] (cts s^{-1})	ME Rate[c] (cts s^{-1})	LE Rate[d] (cts s^{-1})	HE Exp[e] (s)	ME Exp (s)	LE Exp (s)	State
3401	2019-10-07T00:23:37	58763.14	26.6 ± 0.2	5.21 ± 0.06	124.7 ± 0.5	532	1240	562	HSS
3402	2019-10-07T03:41:08	58763.23	28.17 ± 0.09	5.73 ± 0.05	121.4 ± 0.5	3444	2344	599	HSS
3403	2019-10-07T07:12:40	58763.36	21.53 ± 0.11	4.59 ± 0.06	118.3 ± 0.7	1914	1217	239	HSS
3701	2019-10-11T07:47:38	58767.40	27.95 ± 0.09	4.59 ± 0.05	106.7 ± 0.3	3206	2047	1240	HSS
3702	2019-10-11T11:24:31	58767.53	29.07 ± 0.14	5.21 ± 0.05	109.4 ± 0.3	1534	2150	1017	HSS
3802	2019-10-13T23:15:55	58770.05	21.49 ± 0.09	1.95 ± 0.03	97.1 ± 0.2	2602	2095	2028	HSS
3803	2019-10-14T03:00:59	58770.21	14.85 ± 0.09	1.49 ± 0.03	96.6 ± 0.3	1841	1230	1017	HSS
3901	2019-10-16T03:56:56	58772.26	11.25 ± 0.07	0.93 ± 0.02	88.9 ± 0.3	2611	1735	1197	HSS
3902	2019-10-16T07:29:26	58772.40	10.75 ± 0.06	1.09 ± 0.02	89.4 ± 0.2	2920	1950	1676	HSS
4602	2019-10-20T19:37:11	58776.89	24.60 ± 0.12	2.63 ± 0.04	85.3 ± 0.3	1764	1382	1317	HSS
4603	2019-10-20T22:48:00	58777.03	19.57 ± 0.09	2.53 ± 0.04	85.4 ± 0.2	2316	1562	1436	HSS
4701	2019-10-22T06:19:14	58778.35	15.1 ± 0.1	2.48 ± 0.03	81.9 ± 0.2	1516	2122	2095	HSS
4702	2019-10-22T09:47:07	58778.52	11.1 ± 0.1	2.77 ± 0.04	83.6 ± 0.2	1097	2050	2214	HSS
4703	2019-10-22T12:57:58	58778.62	17.6 ± 0.1	2.40 ± 0.04	83.9 ± 0.2	1659	1459	1356	HSS
4801	2019-10-23T23:40:30	58780.07	13.29 ± 0.07	4.24 ± 0.05	81.3 ± 0.2	2534	1702	1616	HSS
4803	2019-10-24T06:18:54	58780.31	20.95 ± 0.12	4.80 ± 0.05	81.4 ± 0.2	1503	1839	1637	HSS
4901	2019-10-25T05:53:35	58781.30	21.25 ± 0.13	4.08 ± 0.04	78.3 ± 0.2	1310	2188	2274	HSS
4902	2019-10-25T09:21:10	58781.48	14.80 ± 0.09	4.59 ± 0.05	78.0 ± 0.2	1655	1866	2211	HSS
4903	2019-10-25T12:32:02	58781.57	22.15 ± 0.14	5.24 ± 0.06	79.7 ± 0.3	1204	1263	898	HSS

Notes.
[a] Exposure ID, e.g., 0101: P0214050*XXXX*, *XXXX* = 0101.
[b] HE: 25–150 keV.
[c] ME: 10–20 keV.
[d] LE: 1–10 keV.
[e] Exposure time.
(This table is available in machine-readable form.)

Guo et al. 2020). We obtained the response files with the tasks *lerspgen*, *merspgen*, and *herspgen*.

We rebinned the spectra to a minimum of 30 counts per bin using the FTOOLS (Blackburn 1995) task *grppha*. We modeled them with XSPEC version 12.10.1[11] (Arnaud 1996). We used the χ^2 statistics, and added a systematic uncertainty of 1.5%. The energy bands adopted for our spectral analysis are: 1.0–10.0 keV (LE), 10.0–30.0 keV (ME), and 30.0–150.0 keV (HE). We jointly fitted the spectra of the three instruments and included a multiplicative constant to account for the relative flux calibration uncertainties (Li et al. 2020). All spectral models include photoelectric absorption, modeled with the *TBabs* and "wilm" abundances (Wilms et al. 2000). The results of our spectral analysis are presented in Section 3.2. We only report results from observations with an exposure time longer than 200 s. All uncertainties are quoted at the 90% confidence level.

3. Results

3.1. Light Curves and Hardness Ratio

Figure 1 shows the long-term light curves in different energy bands and the evolution of the LE hardness ratio (defined as the 4–10 keV count rate divided by the 2–4 keV count rate). The HE and ME count rates show a similar evolution: first, a decrease with time, and then a relatively low, stable level (Figure 1). The LE light curve, however, shows a more complex evolution, with two peaks. The LE count rate rapidly increased after MJD 58697.35, reached a peak value of 220.5 ± 0.4 cts s^{-1} on MJD 58705.53, and then decreased gradually. Then, it increased again during the SIMS, before finally decreasing to a relatively low value (79.7 ± 0.3 cts s^{-1}) during the HSS. We do not know the exact reason for the formation of these two peaks. From the LE hardness ratio, we see that the spectrum gradually softened with time (the bottom panel of Figure 1).

Liu et al. (2021) subdivided the outburst into four spectral states, based on the relative changes in the hardness–intensity diagram and the fractional rms integrated over the 2^{-5}–32 Hz band. In the following spectral analysis, we will adopt their spectral state classification, except for their definition of the LHS. Their preliminary classification was based on hardness ratios and only included the first three Insight-HXMT observations in the LHS. Here, we use spectral analysis to obtain a more accurate classification of this state. We adopt the canonical definition of the LHS as the epochs when the photon index $\Gamma \sim 1.5$–1.7 and the disk flux fraction $f_{\rm dbb} \leqslant 20\%$ (Remillard & McClintock 2006; Belloni 2010). With this definition, the LHS interval includes the first eight Insight-HXMT observations (Section 3.2.1).

3.2. Broadband Spectral Models

3.2.1. `cutoffpl+diskbb` Model

The continuum X-ray emission of BH X-ray binaries generally consists of a thermal/soft and a nonthermal/hard component. The former represents the disk emission and is usually fitted with a multicolor disk-blackbody component (`diskbb` in XSPEC; Mitsuda et al. 1984; Makishima et al. 1986). The latter represents the coronal emission, i.e., it comes

[11] https://heasarc.gsfc.nasa.gov/docs/xanadu/Xspec/

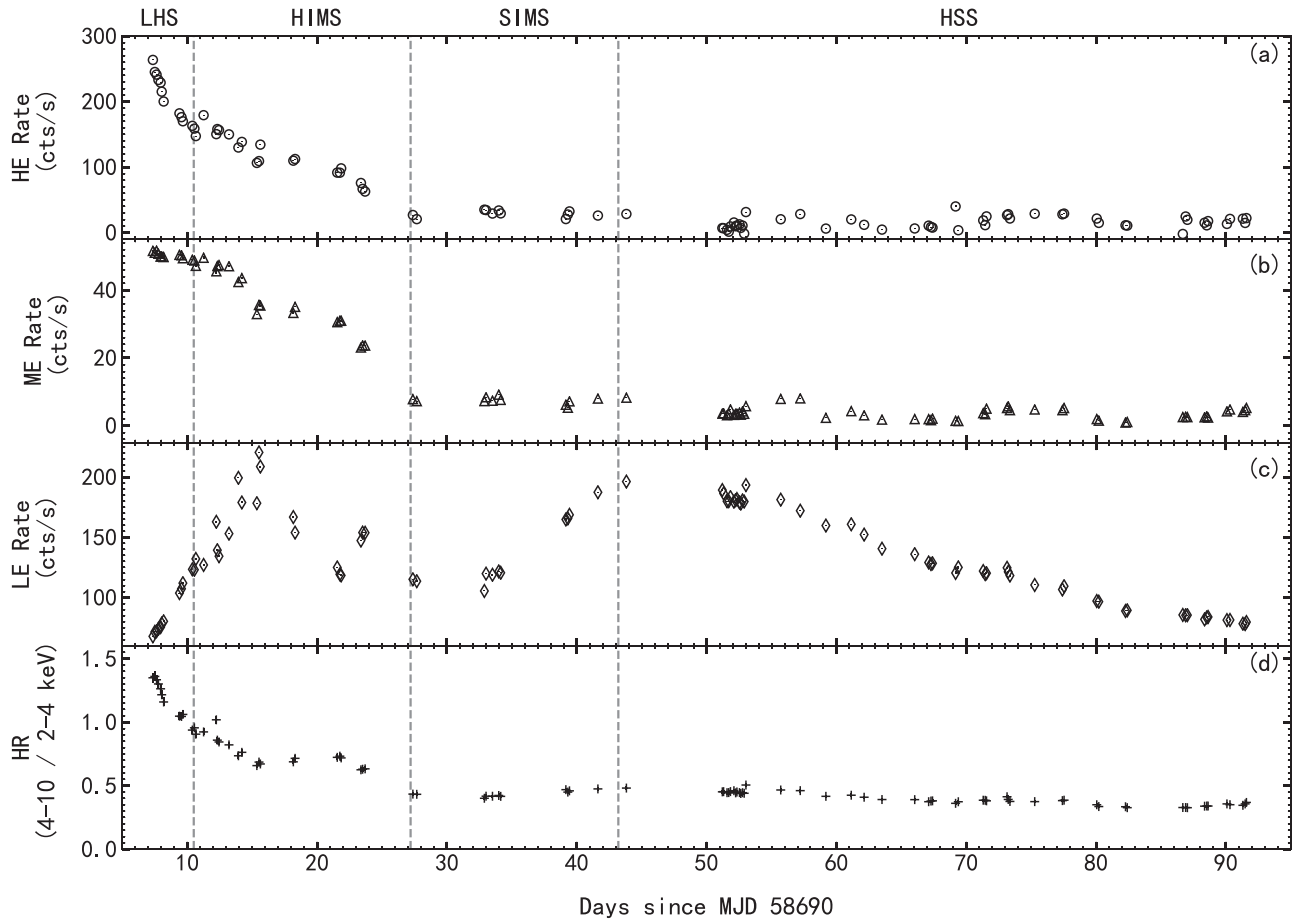

Figure 1. The top three panels show light curves measured with the Insight-HXMT detectors: (a) HE (25–150 keV); (b) ME (10–20 keV); and (c) LE (1–10 keV). Bottom panel (d): the LE hardness ratio (the 4–10 keV count rate over the 2–4 keV count rate). Each data point represents one Insight-HXMT exposure. The spectral state classification follows Liu et al. (2021), except for the definition of the LHS. The state transitions are marked with the dashed lines.

from the Comptonization of disk photons in a hot electron cloud (Eardley et al. 1975; Sunyaev & Titarchuk 1980). It is usually fitted with a power-law component, with or without a high-energy cutoff (`cutoffpl` or `powerlaw`). We tried different combinations of the `cutoffpl` and `diskbb` components in each spectral state (alone or in combination). Based on the F-test probability (the *ftest* command in XSPEC), we found that both components are always present throughout the outburst, with a probability >99.9%.

In some epochs, the fit is improved with the addition of a Gaussian emission line (the energy of the line is limited to between 6.4 and 7 keV) around 6.4–6.6 keV, corresponding to Fe Kα emission. In order to test the significance of this emission line, we followed the approach described in several previous works (Barrière et al. 2015; Bhalerao et al. 2015; Sidoli et al. 2017; Ge et al. 2020; Wang et al. 2021) and used the *simftest*[12] routine in XSPEC, with 10,000 simulations for the observation with the longest exposure time in each spectral state. The probabilities for the line to be required in each state, from the LHS to the HIMS, the SIMS, and the HSS, are P = 98.1%, >99.9%, 99.3%, and 57.7%, respectively, corresponding to significances of 2.35σ, >5σ, 2.7σ, and 0.8σ, respectively. Additionally, we also calculated the ratio between the normalization of the `Gaussian` component and its 1σ error, and we only included the `Gaussian` when the ratio was larger than 3, which was true only at the HIMS. The line significance and the ratio increase if we combine multiple spectra in each state, as shown in Wang et al. (2021). However, we are monitoring the time evolution of the spectra here, and therefore we prefer not to combine them. Hence, we only include the Fe line in our fits to the HIMS spectra. The mean value of the best-fitting central energy of the line in the 18 HIMS epochs (Tables 2 and 3) is $E_{\rm gau} = 6.55$ keV, with a 1σ scatter of 0.15 keV. Thus, the line is consistent with both neutral (6.4 keV) and He-like (6.7 keV) iron.

To check the robustness of our results, we refitted the observation with the longest exposure time in each spectral state with the reflection model `relxill` (Dauser et al. 2013; García et al. 2014) plus `diskbb`. We obtained best-fitting values of $T_{\rm in}$ and $N_{\rm dbb}$ similar to those derived from the simpler model; the latter is therefore preferred. We also fitted some of the LHS and HIMS data with the high-density reflection model `relxillD` to check whether the disk component was really required. For the LHS and HIMS spectra, the `relxillD` component alone gives χ^2/degrees of freedom (dof) = 1451.90/1300 and 1262.59/1326, respectively. Adding a `diskbb` component improves the two fits by $\Delta\chi^2 = 78.82$ and 29.97, respectively, for the loss of 2 dof. The F-test probabilities of 1.85×10^{-16} and 1.24×10^{-7} indicate that the `diskbb` component is significantly required by the LHS and HIMS data. In addition, we compared the best-fitting parameters of the `diskbb` component obtained from the

[12] https://heasarc.gsfc.nasa.gov/xanadu/xspec/manual/node126.html

Table 2
Spectral Fitting Results of EXO 1846–031 Using the `TBabs*(cutoffpl+diskbb)` Model, with $N_{\rm H}$ Fixed at 5.34×10^{22} cm^{-2}

ExpID	Model	Γ	$E_{\rm cut}$ (keV)	$kT_{\rm in}$ (keV)	$N_{\rm dbb}$	$E_{\rm gau}$[c] (keV)	$\sigma_{\rm gau}$[d] (keV)	χ^2/dof	$F_{\rm dbb}$[e]	$F_{\rm pl}$[e]	$f_{\rm dbb}$
0101	CD[a]	$1.39^{+0.04}_{-0.04}$	50^{+3}_{-3}	$1.65^{+0.13}_{-0.16}$	6^{+2}_{-2}	...	...	1280.8/1302	$0.08^{+0.03}_{-0.03}$	$0.705^{+0.007}_{-0.007}$	$0.12^{+0.04}_{-0.04}$
0102	CD	$1.43^{+0.04}_{-0.04}$	50^{+3}_{-3}	$1.5^{+0.2}_{-0.3}$	5^{+4}_{-2}	...	...	1328.6/1443	$0.05^{+0.02}_{-0.02}$	$0.731^{+0.005}_{-0.005}$	$0.07^{+0.03}_{-0.03}$
0103	CD	$1.46^{+0.03}_{-0.04}$	50^{+3}_{-3}	$1.7^{+0.2}_{-0.2}$	4^{+2}_{-2}	...	...	1336.9/1442	$0.06^{+0.03}_{-0.02}$	$0.66^{+0.04}_{-0.04}$	$0.08^{+0.03}_{-0.03}$
0104	CD	$1.49^{+0.04}_{-0.04}$	50^{+5}_{-4}	$1.72^{+0.11}_{-0.12}$	6^{+2}_{-2}	...	...	1388.9/1401	$0.10^{+0.03}_{-0.03}$	$0.779^{+0.006}_{-0.006}$	$0.13^{+0.03}_{-0.03}$
0105	CD	$1.56^{+0.04}_{-0.05}$	50^{+8}_{-7}	$1.6^{+0.3}_{-0.3}$	5^{+5}_{-3}	...	...	1364.9/1470	$0.04^{+0.03}_{-0.02}$	$0.810^{+0.006}_{-0.006}$	$0.05^{+0.03}_{-0.03}$
0106	CD	$1.58^{+0.04}_{-0.04}$	60^{+6}_{-5}	$1.2^{+0.2}_{-0.2}$	17^{+14}_{-7}	...	...	1231.5/1224	$0.07^{+0.03}_{-0.03}$	$0.74^{+0.04}_{-0.05}$	$0.09^{+0.04}_{-0.03}$
0107	CD	$1.65^{+0.06}_{-0.06}$	60^{+14}_{-11}	$1.31^{+0.15}_{-0.16}$	18^{+12}_{-8}	...	...	1222.4/1281	$0.11^{+0.04}_{-0.04}$	$0.73^{+0.05}_{-0.05}$	$0.13^{+0.04}_{-0.04}$
0201	CD	$1.72^{+0.04}_{-0.04}$	50^{+5}_{-4}	$1.10^{+0.09}_{-0.09}$	60^{+20}_{-17}	...	...	1197.2/1342	$0.20^{+0.03}_{-0.03}$	$1.230^{+0.012}_{-0.012}$	$0.16^{+0.03}_{-0.03}$
0301	CDG[b]	$1.86^{+0.04}_{-0.04}$	70^{+9}_{-7}	$1.19^{+0.05}_{-0.05}$	90^{+17}_{-15}	$6.4^{+0.2}_{-p}$	$0.5^{+0.3}_{-0.2}$	1250.3/1325	$0.37^{+0.04}_{-0.04}$	$0.99^{+0.06}_{-0.06}$	$0.27^{+0.03}_{-0.03}$
0302	CDG	$1.72^{+0.06}_{-0.07}$	40^{+6}_{-5}	$1.16^{+0.04}_{-0.05}$	130^{+40}_{-30}	$6.5^{+0.2}_{-0.1}$	$1.2^{+0.3}_{-0.4}$	1232.1/1378	$0.45^{+0.04}_{-0.05}$	$0.80^{+0.09}_{-0.09}$	$0.36^{+0.04}_{-0.04}$
0303	CDG	$1.8^{+0.10}_{-0.06}$	50^{+14}_{-9}	$1.06^{+0.08}_{-0.03}$	200^{+60}_{-70}	$6.4^{+0.4}_{-p}$	$1.6^{+0.3}_{-0.4}$	995.1/1137	$0.47^{+0.07}_{-0.08}$	$0.81^{+0.15}_{-0.13}$	$0.36^{+0.06}_{-0.06}$
0502	CDG	$1.85^{+0.05}_{-0.06}$	50^{+9}_{-7}	$1.15^{+0.04}_{-0.04}$	160^{+40}_{-30}	$6.4^{+0.3}_{-p}$	$1.1^{+0.3}_{-0.4}$	1235.5/1323	$0.56^{+0.05}_{-0.05}$	$0.90^{+0.10}_{-0.11}$	$0.38^{+0.04}_{-0.03}$
0503	CDG	$1.72^{+0.08}_{-0.10}$	40^{+9}_{-7}	$1.12^{+0.04}_{-0.04}$	200^{+50}_{-40}	$6.6^{+0.3}_{-0.1}$	$1.2^{+0.4}_{-0.4}$	1128.0/1264	$0.62^{+0.06}_{-0.06}$	$0.77^{+0.11}_{-0.10}$	$0.45^{+0.05}_{-0.05}$
0601	CDG	$1.95^{+0.08}_{-0.10}$	60^{+30}_{-16}	$1.12^{+0.04}_{-0.05}$	200^{+70}_{-50}	$6.8^{+0.1}_{-0.4}$	$1.1^{+0.6}_{-0.6}$	1268.5/1394	$0.68^{+0.06}_{-0.06}$	$0.93^{+0.13}_{-0.12}$	$0.41^{+0.04}_{-0.04}$
0701	CDG	$1.92^{+0.06}_{-0.06}$	50^{+9}_{-7}	$1.18^{+0.01}_{-0.01}$	300^{+30}_{-20}	$6.7^{+0.1}_{-0.1}$	$0.4^{+0.5}_{-0.2}$	1324.9/1435	$1.28^{+0.04}_{-0.04}$	$0.83^{+0.08}_{-0.10}$	$0.62^{+0.02}_{-0.02}$
0703	CDG	$1.83^{+0.07}_{-0.08}$	40^{+10}_{-7}	$1.17^{+0.02}_{-0.02}$	300^{+30}_{-20}	$6.6^{+0.2}_{-0.2}$	$0.6^{+0.4}_{-0.2}$	1222.0/1351	$1.12^{+0.07}_{-0.07}$	$0.77^{+0.11}_{-0.11}$	$0.62^{+0.04}_{-0.04}$
0802	CDG	$1.71^{+0.14}_{-0.17}$	40^{+7}_{-8}	$1.183^{+0.009}_{-0.009}$	500^{+17}_{-19}	$6.8^{+0.2}_{-0.4}$	$0.9^{+0.3}_{-0.4}$	1328.3/1417	$1.67^{+0.04}_{-0.03}$	$0.62^{+0.05}_{-0.05}$	$0.76^{+0.02}_{-0.02}$
0803	CDG	$1.79^{+0.09}_{-0.23}$	50^{+20}_{-12}	$1.153^{+0.013}_{-0.013}$	500^{+30}_{-30}	$6.4^{+0.4}_{-p}$	...[h]	1214.4/1299	$1.77^{+0.04}_{-0.09}$	$0.33^{+0.10}_{-0.07}$	$0.90^{+0.02}_{-0.06}$
0901	CDG	$1.91^{+0.09}_{-0.11}$	40^{+14}_{-10}	$1.04^{+0.02}_{-0.02}$	500^{+60}_{-50}	$6.6^{+0.3}_{-0.1}$	$0.8^{+0.5}_{-0.4}$	1234.3/1329	$1.12^{+0.06}_{-0.06}$	$0.81^{+0.11}_{-0.19}$	$0.62^{+0.04}_{-0.04}$
0902	CDG	$1.95^{+0.07}_{-0.08}$	66^{+17}_{-12}	$1.05^{+0.02}_{-0.02}$	400^{+50}_{-40}	$6.8^{+0.2}_{-0.2}$	$0.6^{+0.7}_{-0.3}$	1285.6/1423	$0.88^{+0.04}_{-0.04}$	$0.77^{+0.10}_{-0.09}$	$0.53^{+0.03}_{-0.03}$
1001	CDG	$2.08^{+0.05}_{-0.06}$	170^{+170}_{-60}	$0.999^{+0.018}_{-0.014}$	300^{+40}_{-40}	$6.4^{+0.1}_{-p}$	$1.1^{+0.2}_{-0.2}$	1323.7/1469	$0.65^{+0.04}_{-0.03}$	$0.78^{+0.10}_{-0.08}$	$0.45^{+0.03}_{-0.03}$
1002	CDG	$2.15^{+0.05}_{-0.06}$	120^{+60}_{-30}	$0.98^{+0.02}_{-0.02}$	300^{+40}_{-40}	$6.4^{+0.1}_{-p}$	$1.0^{+0.2}_{-0.2}$	1205.3/1424	$0.53^{+0.04}_{-0.04}$	$0.94^{+0.08}_{-0.09}$	$0.37^{+0.03}_{-0.03}$
1003	CDG	$2.09^{+0.10}_{-0.12}$	110^{+200}_{-50}	$0.94^{+0.03}_{-0.03}$	400^{+80}_{-70}	$6.4^{+0.1}_{-p}$	$1.2^{+0.3}_{-0.3}$	1084.8/1256	$0.58^{+0.07}_{-0.07}$	$0.81^{+0.14}_{-0.14}$	$0.42^{+0.06}_{-0.06}$
1101	CDG	$1.95^{+0.08}_{-0.09}$	57^{+17}_{-12}	$1.043^{+0.011}_{-0.012}$	500^{+30}_{-30}	$6.6^{+0.2}_{-0.2}$	$1.2^{+0.1}_{-0.3}$	1281.5/1461	$1.15^{+0.03}_{-0.03}$	$0.46^{+0.07}_{-0.06}$	$0.74^{+0.02}_{-0.03}$
1102	CDG	$1.95^{+0.09}_{-0.10}$	50^{+18}_{-11}	$1.053^{+0.012}_{-0.012}$	500^{+30}_{-30}	$6.5^{+0.2}_{-0.1}$	$0.8^{+0.4}_{-0.3}$	1195.0/1443	$1.23^{+0.04}_{-0.04}$	$0.57^{+0.07}_{-0.15}$	$0.75^{+0.03}_{-0.03}$
1103	CDG	$2.16^{+0.05}_{-0.08}$	500^{+p}_{-300}	$1.082^{+0.012}_{-0.016}$	400^{+40}_{-30}	$6.4^{+0.4}_{-p}$	$1.1^{+0.3}_{-0.5}$	1123.4/1352	$1.14^{+0.04}_{-0.04}$	$0.56^{+0.09}_{-0.08}$	$0.69^{+0.03}_{-0.03}$
1301	CD	$2.0^{+0.09}_{-0.09}$	500[f]	$0.906^{+0.007}_{-0.007}$	900^{+30}_{-30}	...	...	1134.7/1280	$1.188^{+0.011}_{-0.012}$	$0.19^{+0.03}_{-0.03}$	$0.891^{+0.014}_{-0.013}$
1303	CD	$2.2^{+0.2}_{-0.2}$	500[f]	$0.91^{+0.01}_{-0.01}$	900^{+50}_{-50}	...	...	944.3/1125	$1.17^{+0.02}_{-0.02}$	$0.25^{+0.07}_{-0.06}$	$0.87^{+0.03}_{-0.02}$
1501	CD	$1.95^{+0.08}_{-0.08}$	500[f]	$0.900^{+0.006}_{-0.006}$	1000^{+30}_{-30}	...	...	1213.4/1285	$1.273^{+0.009}_{-0.010}$	$0.11^{+0.02}_{-0.02}$	$0.939^{+0.011}_{-0.011}$
1601	CD	$2.05^{+0.06}_{-0.06}$	500[f]	$0.904^{+0.005}_{-0.005}$	1000^{+30}_{-30}	...	...	1322.7/1347	$1.282^{+0.009}_{-0.010}$	$0.20^{+0.02}_{-0.02}$	$0.897^{+0.010}_{-0.010}$
1701	CD	$1.81^{+0.14}_{-0.14}$	500[f]	$0.987^{+0.009}_{-0.010}$	900^{+40}_{-40}	...	...	1047.1/1120	$1.70^{+0.02}_{-0.02}$	$0.15^{+0.04}_{-0.03}$	$0.94^{+0.02}_{-0.02}$
1702	CD	$1.7^{+0.2}_{-0.2}$	500[f]	$0.976^{+0.005}_{-0.006}$	1000^{+30}_{-30}	...	...	1188.9/1242	$1.800^{+0.011}_{-0.011}$	$0.10^{+0.02}_{-0.02}$	$0.981^{+0.009}_{-0.009}$
1703	CD	$1.74^{+0.09}_{-0.20}$	500[f]	$0.981^{+0.004}_{-0.005}$	1000^{+20}_{-20}	...	...	1252.6/1334	$1.803^{+0.009}_{-0.009}$	$0.113^{+0.016}_{-0.013}$	$0.971^{+0.007}_{-0.007}$
1801	CD	$1.87^{+0.06}_{-0.06}$	500[f]	$0.972^{+0.004}_{-0.004}$	1100^{+20}_{-20}	...	...	1615.0/1478	$1.928^{+0.009}_{-0.009}$	$0.24^{+0.03}_{-0.03}$	$0.906^{+0.007}_{-0.007}$
1901	CD	$1.67^{+0.21}_{-0.07}$	500[f]	$1.009^{+0.003}_{-0.003}$	1000^{+14}_{-14}	...	...	1400.2/1433	$2.031^{+0.007}_{-0.007}$	$0.140^{+0.017}_{-0.014}$	$0.970^{+0.005}_{-0.005}$
2201	CD	$1.7^{+0.2}_{-0.3}$	500[f]	$0.991^{+0.005}_{-0.005}$	1100^{+20}_{-20}	...	...	1121.2/1261	$2.014^{+0.011}_{-0.011}$	$0.069^{+0.024}_{-0.015}$	$0.990^{+0.008}_{-0.008}$
2202	CD	$1.59^{+0.27}_{-0.09}$	500[f]	$0.985^{+0.005}_{-0.005}$	1100^{+30}_{-30}	...	...	1129.2/1212	$1.995^{+0.012}_{-0.012}$	$0.073^{+0.020}_{-0.013}$	$0.992^{+0.008}_{-0.008}$
2204	CD	$1.6^{+0.3}_{-0.2}$	500[f]	$0.980^{+0.004}_{-0.004}$	1100^{+20}_{-20}	...	...	1332.5/1241	$1.944^{+0.010}_{-0.010}$	$0.07^{+0.02}_{-0.02}$	$0.994^{+0.008}_{-0.007}$
2205	CD	$1.7^{+0.2}_{-0.2}$	500[f]	$0.986^{+0.003}_{-0.003}$	1100^{+16}_{-16}	...	...	1361.1/1355	$1.935^{+0.007}_{-0.007}$	$0.08^{+0.02}_{-0.02}$	$0.994^{+0.005}_{-0.005}$
2206	CD	$1.7^{+0.3}_{-0.2}$	500[f]	$0.989^{+0.005}_{-0.005}$	1100^{+20}_{-20}	...	...	1219.1/1225	$1.960^{+0.011}_{-0.011}$	$0.09^{+0.03}_{-0.02}$	$0.990^{+0.008}_{-0.008}$
2208	CD	$1.7^{+0.3}_{-0.2}$	500[f]	$0.999^{+0.006}_{-0.006}$	1000^{+30}_{-30}	...	...	1091.1/1192	$1.908^{+0.013}_{-0.013}$	$0.051^{+0.019}_{-0.011}$	$0.994^{+0.010}_{-0.010}$
2209	CD	$1.6^{+0.3}_{-0.2}$	500[f]	$0.987^{+0.004}_{-0.004}$	1100^{+20}_{-20}	...	...	1180.3/1259	$1.931^{+0.010}_{-0.010}$	$0.074^{+0.025}_{-0.013}$	$0.991^{+0.007}_{-0.007}$
2210	CD	$1.8^{+0.2}_{-0.2}$	500[f]	$0.986^{+0.006}_{-0.006}$	1100^{+30}_{-30}	...	...	1151.6/1149	$1.936^{+0.014}_{-0.014}$	$0.08^{+0.03}_{-0.02}$	$0.989^{+0.011}_{-0.010}$
2211	CD	$1.6^{+0.2}_{-0.2}$	500[f]	$0.981^{+0.005}_{-0.005}$	1100^{+30}_{-30}	...	...	1093.9/1196	$1.926^{+0.012}_{-0.012}$	$0.08^{+0.03}_{-0.02}$	$0.990^{+0.009}_{-0.009}$
2212	CD	$1.6^{+0.4}_{-0.2}$	500[f]	$0.982^{+0.003}_{-0.004}$	1100^{+19}_{-18}	...	...	1278.0/1315	$1.925^{+0.008}_{-0.008}$	$0.061^{+0.020}_{-0.013}$	$0.994^{+0.006}_{-0.006}$
2213	CD	$1.6^{+0.3}_{-0.2}$	500[f]	$0.981^{+0.004}_{-0.004}$	1100^{+20}_{-20}	...	...	1189.9/1284	$1.941^{+0.009}_{-0.009}$	$0.08^{+0.02}_{-0.02}$	$0.990^{+0.007}_{-0.007}$
2214	CD	$1.6^{+0.2}_{-0.3}$	500[f]	$0.981^{+0.006}_{-0.006}$	1100^{+30}_{-30}	...	...	989.4/1095	$1.939^{+0.013}_{-0.013}$	$0.06^{+0.03}_{-0.02}$	$0.995^{+0.010}_{-0.010}$
2215	CD	$1.6^{+0.2}_{-0.2}$	500[f]	$0.945^{+0.009}_{-0.009}$	1300^{+50}_{-50}	...	...	1312.9/1159	$1.92^{+0.02}_{-0.03}$	$0.154^{+0.013}_{-0.010}$	$0.902^{+0.013}_{-0.014}$
2301	CD	$1.7^{+0.2}_{-0.1}$	500[f]	$0.990^{+0.004}_{-0.004}$	100^{+17}_{-16}	...	...	1327.1/1407	$1.892^{+0.008}_{-0.008}$	$0.134^{+0.017}_{-0.014}$	$0.965^{+0.006}_{-0.006}$
2401	CD	$1.99^{+0.07}_{-0.07}$	500[f]	$0.965^{+0.004}_{-0.004}$	1100^{+20}_{-19}	...	...	1257.3/1377	$1.797^{+0.009}_{-0.009}$	$0.19^{+0.03}_{-0.03}$	$0.940^{+0.008}_{-0.008}$
2601	CD	$1.6^{+0.3}_{-0.2}$	500[f]	$0.951^{+0.003}_{-0.003}$	1100^{+16}_{-16}	...	...	1422.5/1423	$1.775^{+0.006}_{-0.006}$	$0.08^{+0.06}_{-0.03}$	$0.995^{+0.005}_{-0.005}$
2701	CD	$1.76^{+0.12}_{-0.12}$	500[f]	$0.949^{+0.003}_{-0.003}$	1100^{+17}_{-16}	...	...	1393.7/1464	$1.758^{+0.006}_{-0.006}$	$0.10^{+0.03}_{-0.02}$	$0.981^{+0.006}_{-0.006}$
2801	CD	$1.8^{+0.2}_{-0.3}$	500[f]	$0.938^{+0.003}_{-0.003}$	1200^{+19}_{-19}	...	...	1361.1/1376	$1.703^{+0.007}_{-0.007}$	$0.07^{+0.02}_{-0.02}$	$0.991^{+0.006}_{-0.006}$
2901	CD	$1.7^{+0.3}_{-0.3}$	500[f]	$0.920^{+0.005}_{-0.005}$	1200^{+30}_{-30}	...	...	1120.2/1197	$1.597^{+0.011}_{-0.011}$	$0.045^{+0.028}_{-0.014}$	$0.993^{+0.010}_{-0.010}$
3001	CD	$1.7^{+0.3}_{-0.3}$	500[f]	$0.917^{+0.004}_{-0.005}$	1200^{+30}_{-30}	...	...	1194.6/1238	$1.565^{+0.009}_{-0.009}$	$0.08^{+0.07}_{-0.04}$	$0.993^{+0.009}_{-0.009}$
3102	CD	$1.6^{+0.4}_{-0.3}$	500[f]	$0.900^{+0.004}_{-0.004}$	1200^{+30}_{-30}	...	...	1098.9/1234	$1.532^{+0.01}_{-0.01}$	$0.05^{+0.06}_{-0.02}$	$0.995^{+0.009}_{-0.009}$

Table 2
(Continued)

ExpID	Model	Γ	$E_{\rm cut}$ (keV)	$kT_{\rm in}$ (keV)	$N_{\rm dbb}$	$E_{\rm gau}$[c] (keV)	$\sigma_{\rm gau}$[d] (keV)	χ^2/dof	$F_{\rm dbb}$[e]	$F_{\rm pl}$[e]	$f_{\rm dbb}$
3103	CD	$1.9^{+0.3}_{-0.3}$	500[f]	$0.890^{+0.006}_{-0.006}$	1300^{+40}_{-40}	⋯	⋯	1094.3/1195	$1.537^{+0.011}_{-0.011}$	$0.07^{+0.08}_{-0.03}$	$0.986^{+0.014}_{-0.012}$
3203	CD	$1.8^{+0.5}_{-0.5}$	500[f]	$0.884^{+0.006}_{-0.006}$	1300^{+40}_{-40}	⋯	⋯	1084.7/1177	$1.499^{+0.011}_{-0.011}$	$0.08^{+0.18}_{-0.05}$	$0.993^{+0.013}_{-0.011}$
3301	CD	$1.94^{+0.15}_{-0.15}$	⋯	$0.872^{+0.005}_{-0.005}$	1300^{+30}_{-30}	⋯	⋯	1287.7/1304	$1.427^{+0.009}_{-0.009}$	$0.11^{+0.03}_{-0.02}$	$0.957^{+0.011}_{-0.010}$
3302	CD	$1.8^{+0.2}_{-0.2}$	500[f]	$0.887^{+0.005}_{-0.005}$	1200^{+30}_{-30}	⋯	⋯	1150.9/1277	$1.415^{+0.008}_{-0.008}$	$0.07^{+0.04}_{-0.02}$	$0.981^{+0.010}_{-0.009}$
3303	CD	$1.9^{+0.2}_{-0.2}$	500[f]	$0.882^{+0.007}_{-0.007}$	1200^{+40}_{-40}	⋯	⋯	1079.1/1150	$1.430^{+0.012}_{-0.012}$	$0.09^{+0.05}_{-0.03}$	$0.974^{+0.015}_{-0.013}$
3401	CD	$1.9^{+0.2}_{-0.2}$	500[f]	$0.879^{+0.009}_{-0.009}$	1200^{+60}_{-50}	⋯	⋯	999.4/1150	$1.411^{+0.015}_{-0.015}$	$0.15^{+0.05}_{-0.04}$	$0.93^{+0.02}_{-0.02}$
3402	CD	$1.9^{+0.11}_{-0.11}$	500[f]	$0.868^{+0.008}_{-0.009}$	1300^{+60}_{-50}	⋯	⋯	940.5/1127	$1.386^{+0.015}_{-0.015}$	$0.13^{+0.03}_{-0.03}$	$0.94^{+0.02}_{-0.02}$
3403	CD	$1.7^{+0.2}_{-0.2}$	500[f]	$0.878^{+0.008}_{-0.009}$	1200^{+60}_{-50}	⋯	⋯	973.1/1094	$1.398^{+0.014}_{-0.014}$	$0.060^{+0.019}_{-0.012}$	$0.980^{+0.015}_{-0.015}$
3701	CD	$1.88^{+0.14}_{-0.14}$	500[f]	$0.867^{+0.006}_{-0.006}$	1200^{+40}_{-40}	⋯	⋯	1155.2/1211	$1.253^{+0.010}_{-0.010}$	$0.10^{+0.03}_{-0.02}$	$0.957^{+0.012}_{-0.012}$
3702	CD	$1.92^{+0.13}_{-0.12}$	500[f]	$0.867^{+0.005}_{-0.005}$	1200^{+30}_{-30}	⋯	⋯	1135.6/1309	$1.271^{+0.008}_{-0.008}$	$0.11^{+0.03}_{-0.02}$	$0.949^{+0.01}_{-0.01}$
3802	CD	$2.4^{+0.4}_{-0.4}$	500[f]	$0.843^{+0.007}_{-0.007}$	1200^{+50}_{-60}	⋯	⋯	1091.6/1155	$1.197^{+0.010}_{-0.011}$	$0.17^{+0.14}_{-0.10}$	$0.96^{+0.04}_{-0.02}$
3803	CD	$1.9^{+0.5}_{-0.4}$	500[f]	$0.848^{+0.005}_{-0.006}$	1200^{+20}_{-40}	⋯	⋯	985.5/1151	$1.20^{+0.01}_{-0.01}$	$0.06^{+0.18}_{-0.04}$	$0.992^{+0.015}_{-0.013}$
3901	CD	$3.0^{+0.5}_{-0.6}$	500[f]	$0.845^{+0.007}_{-0.006}$	1100^{+50}_{-60}	⋯	⋯	1008.9/1181	$1.10^{+0.02}_{-0.05}$	$0.3^{+0.5}_{-0.2}$	$0.94^{+0.07}_{-0.05}$
3902	CD	$2.2^{+0.7}_{-0.5}$	500[f]	$0.838^{+0.005}_{-0.005}$	1200^{+30}_{-30}	⋯	⋯	1033.9/1217	$1.132^{+0.008}_{-0.008}$	$0.21^{+0.23}_{-0.15}$	$0.990^{+0.032}_{-0.012}$
4602	CD	$1.6^{+0.3}_{-0.3}$	500[f]	$0.821^{+0.006}_{-0.006}$	1300^{+50}_{-40}	⋯	⋯	1026.0/1209	$1.084^{+0.009}_{-0.009}$	$0.039^{+0.027}_{-0.012}$	$0.983^{+0.013}_{-0.012}$
4603	CD	$1.6^{+0.3}_{-0.2}$	500[f]	$0.825^{+0.006}_{-0.006}$	1300^{+40}_{-40}	⋯	⋯	1124.0/1195	$1.084^{+0.009}_{-0.009}$	$0.033^{+0.016}_{-0.009}$	$0.987^{+0.013}_{-0.012}$
4701	CD	$1.9^{+0.3}_{-0.2}$	500[f]	$0.818^{+0.006}_{-0.006}$	1200^{+40}_{-40}	⋯	⋯	1009.0/1200	$1.032^{+0.008}_{-0.009}$	$0.06^{+0.04}_{-0.02}$	$0.967^{+0.015}_{-0.014}$
4702	CD	$2.3^{+0.3}_{-0.3}$	500[f]	$0.816^{+0.005}_{-0.005}$	1200^{+40}_{-50}	⋯	⋯	1160.7/1320	$1.043^{+0.007}_{-0.008}$	$0.16^{+0.11}_{-0.07}$	$0.94^{+0.03}_{-0.02}$
4703	CD	$2.8^{+0.2}_{-0.3}$	500[f]	$0.822^{+0.009}_{-0.008}$	1100^{+80}_{-80}	⋯	⋯	1110.5/1255	$1.021^{+0.013}_{-0.019}$	$0.29^{+0.11}_{-0.10}$	$0.86^{+0.06}_{-0.05}$
4801	CD	$2.1^{+0.2}_{-0.2}$	500[f]	$0.811^{+0.007}_{-0.007}$	1200^{+50}_{-50}	⋯	⋯	1027.2/1241	$0.979^{+0.010}_{-0.010}$	$0.13^{+0.04}_{-0.03}$	$0.91^{+0.02}_{-0.02}$
4803	CD	$2.1^{+0.2}_{-0.2}$	500[f]	$0.796^{+0.006}_{-0.006}$	1300^{+50}_{-50}	⋯	⋯	1121.5/1261	$0.998^{+0.010}_{-0.010}$	$0.14^{+0.04}_{-0.03}$	$0.91^{+0.02}_{-0.02}$
4901	CD	$2.2^{+0.2}_{-0.2}$	500[f]	$0.807^{+0.005}_{-0.005}$	1200^{+40}_{-40}	⋯	⋯	1180.2/1316	$0.970^{+0.007}_{-0.008}$	$0.13^{+0.05}_{-0.03}$	$0.93^{+0.02}_{-0.02}$
4902	CD	$2.5^{+0.2}_{-0.2}$	500[f]	$0.802^{+0.006}_{-0.006}$	1100^{+50}_{-60}	⋯	⋯	1099.1/1327	$0.932^{+0.011}_{-0.013}$	$0.26^{+0.07}_{-0.06}$	$0.85^{+0.03}_{-0.03}$
4903	CD	$2.1^{+0.2}_{-0.2}$	500[f]	$0.789^{+0.008}_{-0.008}$	1300^{+60}_{-60}	⋯	⋯	1062.9/1197	$0.945^{+0.013}_{-0.015}$	$0.17^{+0.05}_{-0.04}$	$0.88^{+0.02}_{-0.02}$

Notes.
[a] CD: `cutoffpl+diskbb` model.
[b] CDG: `cutoffpl+diskbb+Gaussian` model.
[c] The central energy of the `Gaussian` model.
[d] The line width of the `Gaussian` model.
[e] Units: (10^{-8} erg cm^{-2} s^{-1}).
[f] $E_{\rm cut}$ fixed at 500 keV in the SIMS and the HSS.
[g] The parameter pegs at its lower or upper limit.
[h] This value is unconstrained.

(This table is available in machine-readable form.)

`relxillD+diskbb` model and the simpler model. The best-fitting values of $T_{\rm in}$ and $N_{\rm dbb}$ all vary slightly, $\lesssim$4% and $\lesssim$5%, respectively. Besides, the evolution trends of $T_{\rm in}$ and $N_{\rm dbb}$ from the LHS to the HIMS are all consistent with those derived from the simpler model, thus our main results will not be affected.

We show a representative sample of unfolded spectra (one for each state), together with the corresponding models, in Figure 2.

We set out to determine the evolution of the main physical parameters over the course of the outburst. As the first step of our analysis, we fitted each spectrum with a free absorbing column density parameter $N_{\rm H}$ (the red data points in Figure 3(a)). The best-fitting value of $N_{\rm H}$ is stable in the SIMS and HSS, but there is some scatter in the LHS and HIMS. There is some degeneracy between the best-fitting values of $N_{\rm H}$ and $T_{\rm in}$, which makes it difficult to determine the intrinsic evolution of the disk parameters. To reduce this hindrance, we froze $N_{\rm H}$ at the mean value ($N_{\rm H} \approx 5.34 \times 10^{22}$ cm^{-2}; the red line in Figure 3(a)) derived from the SIMS and HSS fits, and refitted all the spectra with fixed $N_{\rm H}$.

The cutoff energy of the (dominant) power-law component is well constrained for most of the spectra in the LHS and HIMS (Figure 3). In the SIMS and HSS, however, the power-law component weakens: the low-energy spectrum becomes dominated by the `diskbb` component, and the high-energy tail above $\approx$60–70 keV becomes dominated by background counts. For this reason, if we let the cutoff energy vary freely in the fit, most of the times $E_{\rm cut}$ will peg at its upper limit, meaning that a free cutoff energy does not provide a significant improvement to the fit. To better constrain $E_{\rm cut}$ in the HSS, we also tried a simultaneous fit of several spectra near the peak of the outburst, to increase the signal-to-noise ratio. The cutoff energy obtained with this method is formally constrained between 46 and 100 keV. However, the corresponding photon index is only 1.17 ± 0.08, even lower than in the LHS and HIMS, which we regard as unphysical. This contradicts the expectations from the observed evolution (a strong softening) of the hardness ratio from the LHS to the HSS. We suspect that the main reason for this unphysical fitting result is the strong degeneracy between the photon index and the cutoff energy. The two quantities cannot be well constrained simultaneously, after the evolution of the source into the SIMS, and the presence or absence of a cutoff makes no substantial difference to the rest of the spectrum. To keep the model self-consistent

Table 3
Spectral Fitting Results of EXO 1846–031 Using the `TBabs*(simplcut*diskbb)` Model, with $N_{\rm H}$ Fixed at 5.25×10^{22} cm^{-2}

ExpID	Model	Γ	$E_{\rm cut}$ (keV)	k$T_{\rm in}$ (keV)	$N_{\rm dbb}$	$f_{\rm sc}^{g}$	$E_{\rm gau}$[c] (keV)	$\sigma_{\rm gau}$[d] (keV)	χ^2/dof	$F_{\rm dbb}$[e]	$F_{\rm pl}$[e]	$f_{\rm dbb}$
0101	SD[a]	$1.45^{+0.04}_{-0.04}$	60^{+4}_{-3}	$1.02^{+0.15}_{-0.16}$	150^{+120}_{-60}	$0.74^{+0.06}_{-0.06}$	⋯	⋯	1300.6/1302	$0.36^{+0.03}_{-0.03}$	$1.25^{+0.06}_{-0.06}$	$0.22^{+0.02}_{-0.02}$
0102	SD	$1.47^{+0.04}_{-0.04}$	50^{+4}_{-4}	$0.7^{+0.2}_{-0.3}$	600^{+600}_{-300}	$0.85^{+0.06}_{-0.11}$	⋯	⋯	1350.8/1443	$0.30^{+0.03}_{-0.08}$	$1.35^{+0.05}_{-0.09}$	$0.18^{+0.02}_{-0.05}$
0103	SD	$1.53^{+0.02}_{-0.04}$	50^{+3}_{-3}	$0.67^{+0.10}_{-0.06}$	600^{+200}_{-300}	$0.91^{+0.05}_{-0.07}$	⋯	⋯	1358.3/1442	$0.27^{+0.06}_{-0.04}$	$1.32^{+0.07}_{-0.06}$	$0.17^{+0.04}_{-0.03}$
0104	SD	$1.59^{+0.05}_{-0.05}$	60^{+7}_{-6}	$0.8^{+0.2}_{-0.3}$	300^{+400}_{-150}	$0.83^{+0.09}_{-0.09}$	⋯	⋯	1431.5/1401	$0.36^{+0.03}_{-0.06}$	$1.19^{+0.05}_{-0.07}$	$0.23^{+0.02}_{-0.04}$
0105	SD	$1.61^{+0.02}_{-0.02}$	60^{+6}_{-5}	$0.75^{+0.05}_{-0.06}$	500^{+100}_{-100}	$0.75^{+0.06}_{-0.04}$	⋯	⋯	1411.3/1470	$0.25^{+0.12}_{-0.05}$	$1.37^{+0.12}_{-0.07}$	$0.16^{+0.07}_{-0.03}$
0106	SD	$1.60^{+0.04}_{-0.04}$	60^{+6}_{-5}	$0.81^{+0.12}_{-0.12}$	400^{+300}_{-170}	$0.72^{+0.06}_{-0.05}$	⋯	⋯	1238.3/1224	$0.42^{+0.03}_{-0.03}$	$1.25^{+0.05}_{-0.06}$	$0.25^{+0.02}_{-0.02}$
0107	SD	$1.70^{+0.07}_{-0.07}$	70^{+19}_{-13}	$0.76^{+0.11}_{-0.16}$	600^{+400}_{-200}	$0.72^{+0.11}_{-0.07}$	⋯	⋯	1245.7/1281	$0.43^{+0.03}_{-0.04}$	$1.16^{+0.06}_{-0.07}$	$0.27^{+0.02}_{-0.03}$
0201	SD	$1.75^{+0.04}_{-0.04}$	50^{+6}_{-5}	$0.78^{+0.05}_{-0.05}$	800^{+140}_{-170}	$0.62^{+0.04}_{-0.04}$	⋯	⋯	1218.3/1342	$0.64^{+0.02}_{-0.02}$	$1.15^{+0.04}_{-0.04}$	$0.356^{+0.011}_{-0.012}$
0301	SDG[b]	$1.93^{+0.04}_{-0.05}$	80^{+13}_{-10}	$0.93^{+0.04}_{-0.04}$	600^{+100}_{-80}	$0.50^{+0.04}_{-0.04}$	$6.4^{+0.2}_{-p}$	$0.6^{+0.4}_{-0.2}$	1256.9/1325	$0.864^{+0.015}_{-0.016}$	$1.07^{+0.04}_{-0.04}$	$0.446^{+0.012}_{-0.012}$
0302	SDG	$1.76^{+0.07}_{-0.08}$	50^{+8}_{-6}	$1.00^{+0.03}_{-0.03}$	400^{+60}_{-50}	$0.37^{+0.03}_{-0.05}$	$6.5^{+0.2}_{-0.1}$	$1.3^{+0.2}_{-0.3}$	1257.8/1378	$0.857^{+0.013}_{-0.014}$	$1.03^{+0.04}_{-0.04}$	$0.455^{+0.011}_{-0.011}$
0303	SDG	$1.81^{+0.12}_{-0.12}$	50^{+15}_{-10}	$0.96^{+0.04}_{-0.05}$	600^{+120}_{-80}	$0.32^{+0.07}_{-0.06}$	$6.4^{+0.4}_{-p}$	$1.6^{+0.2}_{-0.3}$	1006.9/1137	$0.94^{+0.02}_{-0.02}$	$1.06^{+0.06}_{-0.06}$	$0.47^{+0.02}_{-0.02}$
0502	SDG	$1.94^{+0.06}_{-0.07}$	60^{+14}_{-10}	$0.99^{+0.03}_{-0.03}$	500^{+70}_{-60}	$0.38^{+0.05}_{-0.05}$	$6.6^{+0.3}_{-0.1}$	$1.1^{+0.3}_{-0.3}$	1236.3/1323	$1.056^{+0.014}_{-0.014}$	$0.99^{+0.04}_{-0.04}$	$0.516^{+0.012}_{-0.012}$
0503	SDG	$1.81^{+0.10}_{-0.11}$	50^{+12}_{-9}	$1.00^{+0.04}_{-0.03}$	500^{+60}_{-70}	$0.33^{+0.06}_{-0.06}$	$6.6^{+0.3}_{-0.1}$	$1.2^{+0.3}_{-0.4}$	1130.7/1264	$1.03^{+0.02}_{-0.02}$	$0.96^{+0.05}_{-0.05}$	$0.517^{+0.014}_{-0.014}$
0601	SDG	$2.06^{+0.12}_{-0.14}$	90^{+80}_{-30}	$0.97^{+0.03}_{-0.03}$	700^{+90}_{-70}	$0.34^{+0.06}_{-0.06}$	$6.8^{+0.1}_{-0.4}$	$1.5^{+0.2}_{-0.3}$	1301.4/1394	$1.217^{+0.013}_{-0.013}$	$1.04^{+0.05}_{-0.05}$	$0.540^{+0.013}_{-0.013}$
0701	SDG	$2.21^{+0.07}_{-0.08}$	90^{+40}_{-20}	$1.07^{+0.014}_{-0.014}$	600^{+30}_{-30}	$0.28^{+0.02}_{-0.02}$	$6.7^{+0.1}_{-0.1}$	$0.4^{+0.2}_{-0.4}$	1294.0/1435	$1.758^{+0.010}_{-0.010}$	$0.75^{+0.03}_{-0.03}$	$0.701^{+0.009}_{-0.009}$
0703	SDG	$2.06^{+0.09}_{-0.10}$	70^{+30}_{-16}	$1.07^{+0.02}_{-0.02}$	600^{+40}_{-40}	$0.28^{+0.03}_{-0.03}$	$6.6^{+0.2}_{-0.2}$	$0.1^{+0.1}_{-0.6}$	1216.5/1351	$1.534^{+0.012}_{-0.012}$	$0.78^{+0.04}_{-0.04}$	$0.663^{+0.012}_{-0.012}$
0802	SDG	$2.09^{+0.08}_{-0.09}$	90^{+40}_{-20}	$1.136^{+0.011}_{-0.011}$	600^{+20}_{-20}	$0.16^{+0.02}_{-0.02}$	$6.8^{+0.2}_{-0.4}$	$0.5^{+0.4}_{-0.5}$	1320.0/1417	$2.038^{+0.010}_{-0.010}$	$0.58^{+0.03}_{-0.03}$	$0.778^{+0.009}_{-0.008}$
0803	SDG	$2.12^{+0.11}_{-0.12}$	120^{+190}_{-50}	$1.11^{+0.02}_{-0.02}$	600^{+40}_{-30}	$0.17^{+0.02}_{-0.02}$	$6.4^{+0.4}_{-p}$	$0.1^{+4.2}_{-0.1}$	1209.3/1299	$1.933^{+0.013}_{-0.013}$	$0.59^{+0.04}_{-0.04}$	$0.766^{+0.014}_{-0.013}$
0901	SDG	$1.93^{+0.13}_{-0.16}$	50^{+20}_{-12}	$0.97^{+0.02}_{-0.02}$	800^{+60}_{-60}	$0.20^{+0.04}_{-0.05}$	$6.6^{+0.3}_{-0.1}$	$1.1^{+0.4}_{-0.5}$	1262.7/1329	$1.515^{+0.012}_{-0.012}$	$0.69^{+0.04}_{-0.04}$	$0.687^{+0.013}_{-0.012}$
0902	SDG	$2.10^{+0.07}_{-0.07}$	90^{+40}_{-20}	$0.94^{+0.04}_{-0.02}$	800^{+60}_{-100}	$0.31^{+0.03}_{-0.12}$	$6.8^{+0.2}_{-0.2}$	$0.4^{+1.2}_{-0.4}$	1325.2/1423	$1.356^{+0.009}_{-0.009}$	$0.79^{+0.03}_{-0.03}$	$0.632^{+0.010}_{-0.010}$
1001	SDG	$2.18^{+0.04}_{-0.07}$	400^{+p}_{-200}	$0.90^{+0.02}_{-0.02}$	800^{+60}_{-60}	$0.31^{+0.03}_{-0.04}$	$6.4^{+0.1}_{-p}$	$1.1^{+0.2}_{-0.2}$	1373.2/1469	$1.109^{+0.007}_{-0.007}$	$0.79^{+0.03}_{-0.03}$	$0.584^{+0.008}_{-0.008}$
1002	SDG	$2.19^{+0.08}_{-0.08}$	140^{+120}_{-50}	$0.85^{+0.02}_{-0.02}$	1000^{+120}_{-90}	$0.35^{+0.05}_{-0.04}$	$6.6^{+0.2}_{-0.1}$	$1.1^{+0.2}_{-0.2}$	1303.8/1424	$1.033^{+0.009}_{-0.010}$	$0.76^{+0.03}_{-0.03}$	$0.577^{+0.011}_{-0.011}$
1003	SDG	$2.03^{+0.16}_{-0.19}$	80^{+150}_{-40}	$0.87^{+0.03}_{-0.04}$	900^{+160}_{-120}	$0.26^{+0.07}_{-0.06}$	$6.4^{+0.1}_{-p}$	$1.3^{+0.2}_{-0.3}$	1117.2/1256	$1.044^{+0.014}_{-0.014}$	$0.75^{+0.06}_{-0.05}$	$0.58^{+0.02}_{-0.02}$
1101	SDG	$2.03^{+0.10}_{-0.11}$	70^{+30}_{-17}	$1.001^{+0.011}_{-0.010}$	700^{+30}_{-30}	$0.14^{+0.02}_{-0.02}$	$6.6^{+0.2}_{-0.2}$	$1.2^{+0.2}_{-0.2}$	1289.1/1461	$1.433^{+0.007}_{-0.007}$	$0.46^{+0.02}_{-0.02}$	$0.756^{+0.009}_{-0.009}$
1102	SDG	$2.09^{+0.12}_{-0.14}$	70^{+40}_{-20}	$1.001^{+0.012}_{-0.011}$	700^{+30}_{-30}	$0.17^{+0.03}_{-0.03}$	$6.4^{+0.2}_{-p}$	$0.8^{+0.4}_{-0.3}$	1222.9/1443	$1.482^{+0.008}_{-0.008}$	$0.47^{+0.03}_{-0.03}$	$0.760^{+0.011}_{-0.010}$
1103	SDG	$2.20^{+0.07}_{-0.08}$	500^{+p}_{-300}	$1.021^{+0.012}_{-0.013}$	700^{+30}_{-30}	$0.15^{+0.02}_{-0.02}$	$6.4^{+0.4}_{-p}$	$1.2^{+0.2}_{-0.3}$	1149.3/1352	$1.489^{+0.009}_{-0.009}$	$0.48^{+0.03}_{-0.03}$	$0.755^{+0.012}_{-0.012}$
1301	SD	$2.01^{+0.09}_{-0.09}$	500[f]	$0.900^{+0.008}_{-0.008}$	1000^{+40}_{-40}	$0.054^{+0.008}_{-0.007}$	⋯	⋯	1147.3/1280	$1.384^{+0.01}_{-0.01}$	$0.20^{+0.03}_{-0.03}$	$0.87^{+0.02}_{-0.02}$
1303	SD	$2.3^{+0.2}_{-0.2}$	500[f]	$0.898^{+0.012}_{-0.012}$	1000^{+60}_{-60}	$0.066^{+0.018}_{-0.014}$	⋯	⋯	947.5/1125	$1.363^{+0.014}_{-0.014}$	$0.15^{+0.04}_{-0.03}$	$0.90^{+0.02}_{-0.02}$
1501	SD	$1.95^{+0.09}_{-0.08}$	500[f]	$0.898^{+0.007}_{-0.007}$	1000^{+40}_{-40}	$0.029^{+0.005}_{-0.005}$	⋯	⋯	1229.0/1285	$1.457^{+0.01}_{-0.01}$	$0.13^{+0.02}_{-0.02}$	$0.920^{+0.013}_{-0.012}$
1601	SD	$2.06^{+0.07}_{-0.06}$	500[f]	$0.899^{+0.006}_{-0.006}$	1100^{+30}_{-30}	$0.050^{+0.005}_{-0.005}$	⋯	⋯	1338.5/1347	$1.492^{+0.009}_{-0.009}$	$0.18^{+0.02}_{-0.02}$	$0.893^{+0.011}_{-0.011}$
1701	SD	$1.82^{+0.15}_{-0.14}$	500[f]	$0.985^{+0.010}_{-0.011}$	1000^{+50}_{-40}	$0.027^{+0.008}_{-0.007}$	⋯	⋯	1048.9/1120	$1.92^{+0.02}_{-0.02}$	$0.20^{+0.05}_{-0.04}$	$0.91^{+0.02}_{-0.02}$
1702	SD	$1.65^{+0.15}_{-0.15}$	500[f]	$0.977^{+0.006}_{-0.006}$	1000^{+30}_{-30}	$0.011^{+0.003}_{-0.003}$	⋯	⋯	1210.6/1242	$2.001^{+0.012}_{-0.012}$	$0.15^{+0.03}_{-0.03}$	$0.930^{+0.014}_{-0.012}$
1703	SD	$1.73^{+0.10}_{-0.10}$	500[f]	$0.982^{+0.005}_{-0.005}$	1000^{+20}_{-20}	$0.015^{+0.003}_{-0.002}$	⋯	⋯	1283.4/1334	$2.011^{+0.010}_{-0.010}$	$0.18^{+0.03}_{-0.02}$	$0.920^{+0.011}_{-0.010}$
1801	SD	$1.90^{+0.07}_{-0.07}$	500[f]	$0.967^{+0.005}_{-0.005}$	1200^{+30}_{-20}	$0.055^{+0.005}_{-0.004}$	⋯	⋯	1650.3/1478	$2.197^{+0.008}_{-0.008}$	$0.39^{+0.04}_{-0.03}$	$0.851^{+0.012}_{-0.011}$
1901	SD	$1.76^{+0.18}_{-0.08}$	500[f]	$1.010^{+0.004}_{-0.004}$	1000^{+17}_{-16}	$0.016^{+0.002}_{-0.002}$	⋯	⋯	1466.7/1433	$2.260^{+0.008}_{-0.008}$	$0.19^{+0.02}_{-0.02}$	$0.922^{+0.008}_{-0.008}$
2201	SD	$1.62^{+0.24}_{-0.24}$	500[f]	$0.993^{+0.005}_{-0.005}$	1100^{+30}_{-20}	$0.006^{+0.003}_{-0.002}$	⋯	⋯	1134.4/1261	$2.231^{+0.012}_{-0.012}$	$0.10^{+0.03}_{-0.03}$	$0.957^{+0.014}_{-0.011}$
2202	SD	$1.6^{+0.2}_{-0.3}$	500[f]	$0.987^{+0.005}_{-0.005}$	1100^{+30}_{-30}	$0.005^{+0.002}_{-0.001}$	⋯	⋯	1140.3/1212	$2.210^{+0.013}_{-0.013}$	$0.11^{+0.03}_{-0.03}$	$0.951^{+0.013}_{-0.012}$
2204	SD	$1.6^{+0.2}_{-0.2}$	500[f]	$0.981^{+0.004}_{-0.004}$	1100^{+20}_{-20}	$0.003^{+0.001}_{-0.001}$	⋯	⋯	1365.4/1241	$2.154^{+0.012}_{-0.012}$	$0.09^{+0.03}_{-0.03}$	$0.958^{+0.015}_{-0.012}$
2205	SD	$1.7^{+0.3}_{-0.3}$	500[f]	$0.988^{+0.003}_{-0.003}$	1100^{+20}_{-20}	$0.004^{+0.001}_{-0.001}$	⋯	⋯	1413.3/1355	$2.142^{+0.008}_{-0.008}$	$0.13^{+0.02}_{-0.03}$	$0.941^{+0.007}_{-0.013}$
2206	SD	$1.6^{+0.2}_{-0.2}$	500[f]	$0.990^{+0.005}_{-0.005}$	1100^{+30}_{-20}	$0.006^{+0.002}_{-0.001}$	⋯	⋯	1241.5/1225	$2.171^{+0.013}_{-0.013}$	$0.13^{+0.03}_{-0.03}$	$0.945^{+0.014}_{-0.012}$
2208	SD	$1.58^{+0.14}_{-0.26}$	500[f]	$1.002^{+0.006}_{-0.006}$	1000^{+30}_{-30}	$0.004^{+0.002}_{-0.001}$	⋯	⋯	1106.1/1192	$2.109^{+0.015}_{-0.015}$	$0.13^{+0.03}_{-0.05}$	$0.942^{+0.013}_{-0.021}$
2209	SD	$1.7^{+0.2}_{-0.2}$	500[f]	$0.989^{+0.004}_{-0.004}$	1100^{+20}_{-20}	$0.005^{+0.002}_{-0.001}$	⋯	⋯	1202.7/1259	$2.139^{+0.012}_{-0.011}$	$0.10^{+0.03}_{-0.02}$	$0.956^{+0.012}_{-0.011}$
2210	SD	$1.6^{+0.2}_{-0.2}$	500[f]	$0.987^{+0.006}_{-0.006}$	1100^{+30}_{-30}	$0.006^{+0.003}_{-0.002}$	⋯	⋯	1163.5/1149	$2.15^{+0.02}_{-0.02}$	$0.10^{+0.03}_{-0.03}$	$0.957^{+0.014}_{-0.013}$
2211	SD	$1.7^{+0.2}_{-0.2}$	500[f]	$0.982^{+0.005}_{-0.005}$	1100^{+30}_{-30}	$0.006^{+0.002}_{-0.002}$	⋯	⋯	1109.4/1196	$2.136^{+0.014}_{-0.014}$	$0.10^{+0.03}_{-0.03}$	$0.955^{+0.013}_{-0.012}$
2212	SD	$1.7^{+0.2}_{-0.3}$	500[f]	$0.984^{+0.004}_{-0.004}$	1100^{+20}_{-20}	$0.004^{+0.001}_{-0.001}$	⋯	⋯	1301.9/1315	$2.133^{+0.010}_{-0.010}$	$0.09^{+0.03}_{-0.02}$	$0.961^{+0.012}_{-0.010}$
2213	SD	$1.7^{+0.3}_{-0.2}$	500[f]	$0.983^{+0.004}_{-0.004}$	1100^{+20}_{-20}	$0.006^{+0.002}_{-0.001}$	⋯	⋯	1221.2/1284	$2.151^{+0.011}_{-0.011}$	$0.11^{+0.03}_{-0.02}$	$0.952^{+0.012}_{-0.010}$
2214	SD	$1.6^{+0.2}_{-0.2}$	500[f]	$0.982^{+0.005}_{-0.005}$	1100^{+30}_{-30}	$0.004^{+0.001}_{-0.001}$	⋯	⋯	994.4/1095	$2.15^{+0.02}_{-0.02}$	$0.16^{+0.02}_{-0.06}$	$0.932^{+0.010}_{-0.024}$
2215	SD	$1.6^{+0.3}_{-0.2}$	500[f]	$0.946^{+0.009}_{-0.010}$	1300^{+60}_{-50}	$0.047^{+0.009}_{-0.004}$	⋯	⋯	1323.5/1159	$2.22^{+0.02}_{-0.02}$	$0.05^{+0.05}_{-0.11}$	$0.98^{+0.02}_{-0.05}$
2301	SD	$1.71^{+0.18}_{-0.08}$	500[f]	$0.991^{+0.004}_{-0.004}$	1000^{+20}_{-20}	$0.018^{+0.003}_{-0.002}$	⋯	⋯	1357.7/1407	$2.114^{+0.008}_{-0.008}$	$0.18^{+0.02}_{-0.02}$	$0.922^{+0.009}_{-0.008}$
2401	SD	$1.99^{+0.08}_{-0.08}$	500[f]	$0.963^{+0.005}_{-0.005}$	1100^{+30}_{-30}	$0.032^{+0.004}_{-0.004}$	⋯	⋯	1284.8/1377	$2.028^{+0.009}_{-0.009}$	$0.17^{+0.02}_{-0.02}$	$0.921^{+0.009}_{-0.008}$
2601	SD	$1.8^{+0.2}_{-0.3}$	500[f]	$0.953^{+0.003}_{-0.003}$	1100^{+20}_{-20}	$0.003^{+0.001}_{-0.001}$	⋯	⋯	1467.1/1423	$1.974^{+0.008}_{-0.008}$	$0.06^{+0.02}_{-0.02}$	$0.969^{+0.012}_{-0.009}$
2701	SD	$1.71^{+0.23}_{-0.12}$	500[f]	$0.951^{+0.003}_{-0.004}$	1100^{+20}_{-20}	$0.010^{+0.002}_{-0.002}$	⋯	⋯	1433.3/1464	$1.960^{+0.007}_{-0.007}$	$0.10^{+0.02}_{-0.02}$	$0.951^{+0.009}_{-0.008}$
2801	SD	$1.72^{+0.18}_{-0.18}$	500[f]	$0.940^{+0.003}_{-0.003}$	1100^{+20}_{-20}	$0.005^{+0.002}_{-0.001}$	⋯	⋯	1393.1/1376	$1.898^{+0.008}_{-0.008}$	$0.08^{+0.02}_{-0.02}$	$0.960^{+0.010}_{-0.009}$
2901	SD	$1.7^{+0.3}_{-0.3}$	500[f]	$0.922^{+0.005}_{-0.005}$	1200^{+30}_{-30}	$0.004^{+0.002}_{-0.001}$	⋯	⋯	1144.1/1197	$1.787^{+0.013}_{-0.013}$	$0.04^{+0.02}_{-0.02}$	$0.979^{+0.012}_{-0.011}$
3001	SD	$1.7^{+0.2}_{-0.4}$	500[f]	$0.918^{+0.004}_{-0.005}$	1200^{+30}_{-30}	$0.004^{+0.003}_{-0.001}$	⋯	⋯	1214.8/1238	$1.750^{+0.011}_{-0.011}$	$0.05^{+0.02}_{-0.02}$	$0.974^{+0.012}_{-0.011}$
3102	SD	$1.7^{+0.3}_{-0.4}$	500[f]	$0.901^{+0.004}_{-0.004}$	1200^{+30}_{-30}	$0.003^{+0.002}_{-0.001}$	⋯	⋯	1110.8/1234	$1.718^{+0.012}_{-0.012}$	$0.03^{+0.02}_{-0.02}$	$0.983^{+0.013}_{-0.011}$

Table 3
(Continued)

ExpID	Model	Γ	$E_{\rm cut}$ (keV)	k$T_{\rm in}$ (keV)	$N_{\rm dbb}$	$f_{\rm sc}^{g}$	$E_{\rm gau}$[c] (keV)	$\sigma_{\rm gau}$[d] (keV)	χ^2/dof	$F_{\rm dbb}$[e]	$F_{\rm pl}$[e]	$f_{\rm dbb}$
3103	SD	$1.9^{+0.3}_{-0.3}$	500[f]	$0.891^{+0.006}_{-0.007}$	1300^{+50}_{-40}	$0.009^{+0.006}_{-0.004}$	⋯	⋯	1093.6/1195	$1.727^{+0.014}_{-0.013}$	$0.05^{+0.03}_{-0.02}$	$0.972^{+0.016}_{-0.014}$
3203	SD	$1.7^{+0.5}_{-0.3}$	500[f]	$0.885^{+0.006}_{-0.006}$	1300^{+40}_{-40}	$0.004^{+0.005}_{-0.002}$	⋯	⋯	1095.1/1177	$1.685^{+0.013}_{-0.013}$	$0.04^{+0.04}_{-0.03}$	$0.978^{+0.020}_{-0.014}$
3301	SD	$1.92^{+0.15}_{-0.15}$	500[f]	$0.872^{+0.006}_{-0.006}$	1300^{+40}_{-40}	$0.023^{+0.005}_{-0.004}$	⋯	⋯	1290.4/1304	$1.62^{+0.01}_{-0.01}$	$0.12^{+0.03}_{-0.03}$	$0.931^{+0.016}_{-0.014}$
3302	SD	$1.8^{+0.2}_{-0.2}$	500[f]	$0.889^{+0.005}_{-0.005}$	1200^{+40}_{-30}	$0.011^{+0.004}_{-0.003}$	⋯	⋯	1152.6/1277	$1.59^{+0.01}_{-0.01}$	$0.07^{+0.03}_{-0.02}$	$0.955^{+0.015}_{-0.012}$
3303	SD	$1.9^{+0.2}_{-0.2}$	500[f]	$0.883^{+0.007}_{-0.007}$	1200^{+50}_{-50}	$0.014^{+0.006}_{-0.004}$	⋯	⋯	1084.2/1150	$1.615^{+0.014}_{-0.014}$	$0.07^{+0.03}_{-0.03}$	$0.96^{+0.02}_{-0.02}$
3401	SD	$1.8^{+0.2}_{-0.2}$	500[f]	$0.879^{+0.011}_{-0.011}$	1300^{+70}_{-60}	$0.036^{+0.009}_{-0.007}$	⋯	⋯	1005.8/1150	$1.61^{+0.02}_{-0.02}$	$0.22^{+0.07}_{-0.05}$	$0.88^{+0.03}_{-0.03}$
3402	SD	$1.9^{+0.12}_{-0.11}$	500[f]	$0.868^{+0.009}_{-0.009}$	1300^{+70}_{-60}	$0.031^{+0.006}_{-0.006}$	⋯	⋯	952.9/1127	$1.59^{+0.02}_{-0.02}$	$0.17^{+0.04}_{-0.04}$	$0.91^{+0.02}_{-0.02}$
3403	SD	$1.7^{+0.2}_{-0.2}$	500[f]	$0.879^{+0.009}_{-0.009}$	1200^{+60}_{-60}	$0.011^{+0.004}_{-0.003}$	⋯	⋯	981.4/1094	$1.58^{+0.02}_{-0.02}$	$0.14^{+0.06}_{-0.04}$	$0.92^{+0.03}_{-0.02}$
3701	SD	$1.87^{+0.14}_{-0.14}$	500[f]	$0.867^{+0.007}_{-0.007}$	1200^{+50}_{-40}	$0.023^{+0.005}_{-0.005}$	⋯	⋯	1169.9/1211	$1.426^{+0.011}_{-0.011}$	$0.12^{+0.03}_{-0.03}$	$0.93^{+0.02}_{-0.02}$
3702	SD	$1.89^{+0.13}_{-0.12}$	500[f]	$0.867^{+0.006}_{-0.006}$	1200^{+40}_{-40}	$0.027^{+0.005}_{-0.004}$	⋯	⋯	1155.1/1309	$1.448^{+0.009}_{-0.009}$	$0.13^{+0.03}_{-0.02}$	$0.917^{+0.016}_{-0.014}$
3802	SD	$2.2^{+0.4}_{-0.4}$	500[f]	$0.843^{+0.008}_{-0.008}$	1300^{+60}_{-60}	$0.016^{+0.011}_{-0.007}$	⋯	⋯	1096.9/1155	$1.360^{+0.013}_{-0.013}$	$0.04^{+0.02}_{-0.02}$	$0.97^{+0.02}_{-0.02}$
3803	SD	$1.9^{+0.5}_{-0.4}$	500[f]	$0.849^{+0.006}_{-0.006}$	1200^{+40}_{-40}	$0.004^{+0.004}_{-0.002}$	⋯	⋯	995.1/1151	$1.360^{+0.012}_{-0.012}$	$0.02^{+0.02}_{-0.02}$	$0.985^{+0.016}_{-0.014}$
3901	SD	$2.9^{+0.6}_{-0.7}$	500[f]	$0.842^{+0.006}_{-0.008}$	1200^{+50}_{-40}	$0.012^{+0.021}_{-0.008}$	⋯	⋯	1014.5/1181	$1.262^{+0.011}_{-0.010}$	$0.01^{+0.02}_{-0.02}$	$0.992^{+0.013}_{-0.012}$
3902	SD	$2.0^{+0.6}_{-0.5}$	500[f]	$0.839^{+0.005}_{-0.005}$	1200^{+40}_{-40}	$0.005^{+0.006}_{-0.003}$	⋯	⋯	1047.0/1217	$1.285^{+0.010}_{-0.010}$	$0.02^{+0.02}_{-0.02}$	$0.988^{+0.013}_{-0.012}$
4602	SD	$1.6^{+0.3}_{-0.3}$	500[f]	$0.823^{+0.006}_{-0.006}$	1300^{+50}_{-50}	$0.008^{+0.004}_{-0.003}$	⋯	⋯	1028.6/1209	$1.235^{+0.011}_{-0.011}$	$0.07^{+0.04}_{-0.03}$	$0.95^{+0.03}_{-0.02}$
4603	SD	$1.7^{+0.2}_{-0.3}$	500[f]	$0.827^{+0.006}_{-0.006}$	1200^{+50}_{-40}	$0.007^{+0.003}_{-0.002}$	⋯	⋯	1127.4/1195	$1.233^{+0.011}_{-0.011}$	$0.06^{+0.03}_{-0.03}$	$0.95^{+0.03}_{-0.02}$
4701	SD	$1.8^{+0.2}_{-0.2}$	500[f]	$0.820^{+0.007}_{-0.007}$	1200^{+50}_{-50}	$0.015^{+0.006}_{-0.004}$	⋯	⋯	1010.6/1200	$1.182^{+0.011}_{-0.011}$	$0.07^{+0.03}_{-0.02}$	$0.94^{+0.02}_{-0.02}$
4702	SD	$2.0^{+0.2}_{-0.2}$	500[f]	$0.816^{+0.006}_{-0.006}$	1300^{+40}_{-40}	$0.023^{+0.007}_{-0.005}$	⋯	⋯	1189.3/1320	$1.201^{+0.008}_{-0.008}$	$0.07^{+0.02}_{-0.02}$	$0.943^{+0.018}_{-0.015}$
4703	SD	$2.4^{+0.3}_{-0.3}$	500[f]	$0.810^{+0.007}_{-0.008}$	1300^{+60}_{-50}	$0.038^{+0.016}_{-0.011}$	⋯	⋯	1130.8/1255	$1.195^{+0.010}_{-0.010}$	$0.06^{+0.02}_{-0.02}$	$0.955^{+0.016}_{-0.014}$
4801	SD	$2.1^{+0.2}_{-0.2}$	500[f]	$0.808^{+0.008}_{-0.008}$	1300^{+60}_{-50}	$0.040^{+0.009}_{-0.007}$	⋯	⋯	1039.6/1241	$1.144^{+0.010}_{-0.010}$	$0.11^{+0.03}_{-0.02}$	$0.91^{+0.02}_{-0.02}$
4803	SD	$2.02^{+0.15}_{-0.15}$	500[f]	$0.794^{+0.007}_{-0.007}$	1400^{+60}_{-60}	$0.040^{+0.008}_{-0.007}$	⋯	⋯	1132.0/1261	$1.173^{+0.011}_{-0.010}$	$0.13^{+0.03}_{-0.03}$	$0.90^{+0.02}_{-0.02}$
4901	SD	$2.1^{+0.2}_{-0.2}$	500[f]	$0.805^{+0.006}_{-0.006}$	1300^{+50}_{-50}	$0.033^{+0.008}_{-0.006}$	⋯	⋯	1192.4/1316	$1.125^{+0.008}_{-0.008}$	$0.08^{+0.02}_{-0.02}$	$0.934^{+0.016}_{-0.014}$
4902	SD	$2.3^{+0.2}_{-0.2}$	500[f]	$0.792^{+0.007}_{-0.007}$	1300^{+60}_{-50}	$0.058^{+0.012}_{-0.010}$	⋯	⋯	1123.0/1327	$1.111^{+0.009}_{-0.009}$	$0.10^{+0.02}_{-0.02}$	$0.920^{+0.015}_{-0.014}$
4903	SD	$2.0^{+0.2}_{-0.2}$	500[f]	$0.786^{+0.009}_{-0.009}$	1400^{+80}_{-70}	$0.052^{+0.012}_{-0.010}$	⋯	⋯	1074.9/1197	$1.126^{+0.012}_{-0.012}$	$0.16^{+0.04}_{-0.03}$	$0.88^{+0.03}_{-0.02}$

Notes.
[a] SD: `simplcut*diskbb` model.
[b] SDG: `simplcut*diskbb+Gaussian` model.
[c] The central energy of the `Gaussian` model.
[d] The line width of the `Gaussian` model.
[e] Units: (10^{-8} erg cm^{-2} s^{-1}).
[f] $E_{\rm cut}$ fixed at 500 keV in the SIMS and HSS.
[g] Refers to reaching the lower or upper limit.
[h] $f_{\rm sc}$ is the scattered fraction, i.e., the proportion of disk photons scattered by the corona.

(This table is available in machine-readable form.)

throughout the outburst evolution, we fixed $E_{\rm cut}$ at 500 keV in the SIMS and HSS. The photon index then increases to ≈2, which is more consistent with the typical value of the photon index in the soft state. In addition, other parameters, such as $T_{\rm in}$ (≈1 keV), the fraction of the `diskbb` component (⩾90%), and the fraction of the `cutoffpl` component (⩽10%), at this time are all in the canonical range of the soft state.

We show the best-fitting parameters (Table 2) of the `cutoffpl+diskbb` model (with the assumed constant $N_{\rm H}$), as well as the unabsorbed bolometric disk flux, the power-law flux, and the ratio between the disk flux and the total flux, as the red dots in Figure 3. The four parameters of interest are the power-law photon index, the cutoff energy (only in the LHS and HIMS), the inner disk radius, and the peak disk temperature.

The photon index Γ gradually increased from ≈1.4 to ≈2.2 as the source evolved from the LHS to the HIMS, and then remained almost constant within the uncertainties in the SIMS and HSS.

$E_{\rm cut}$ fluctuated between ≈40 and ≈90 keV when the source was in the LHS and the HIMS, except for the last few observations of the HIMS. As mentioned above, it was unconstrained in the SIMS and the HSS, and was fixed at 500 keV for fitting purposes in XSPEC; we did not plot such data points, as shown in Figure 3(c).

The inner disk color temperature $T_{\rm in}$ unexpectedly decreased during the LHS. It remained approximately constant around 1 keV throughout the HIMS. Finally, it gradually decreased (as expected) during the outburst decline in the HSS.

The apparent inner radius of the accretion disk, $r_{\rm in}$ ($\propto\sqrt{N_{\rm dbb}}$, where $N_{\rm dbb}$ is the `diskbb` normalization), unexpectedly increased during the LHS and HIMS. This is seemingly inconsistent with the canonical scenario that the inner disk moves toward the ISCO during those states (Remillard & McClintock 2006; Muñoz-Darias et al. 2011; Tao et al. 2015). We will suggest a possible explanation in Section 3.3. After reaching its peak in the SIMS, $r_{\rm in}$ remained mostly constant throughout the HSS, apart from a slight increasing trend (only by ∼10%) near the end of that state. We interpret the evolution of $r_{\rm in}$ as evidence that the disk had reached a steady state (the Shakura–Sunyaev solution) and the inner disk radius had settled at the ISCO at the beginning of the HSS.

The unabsorbed disk flux $F_{\rm dbb}$ increased rapidly and then decreased slowly in the LHS and HIMS, before starting to

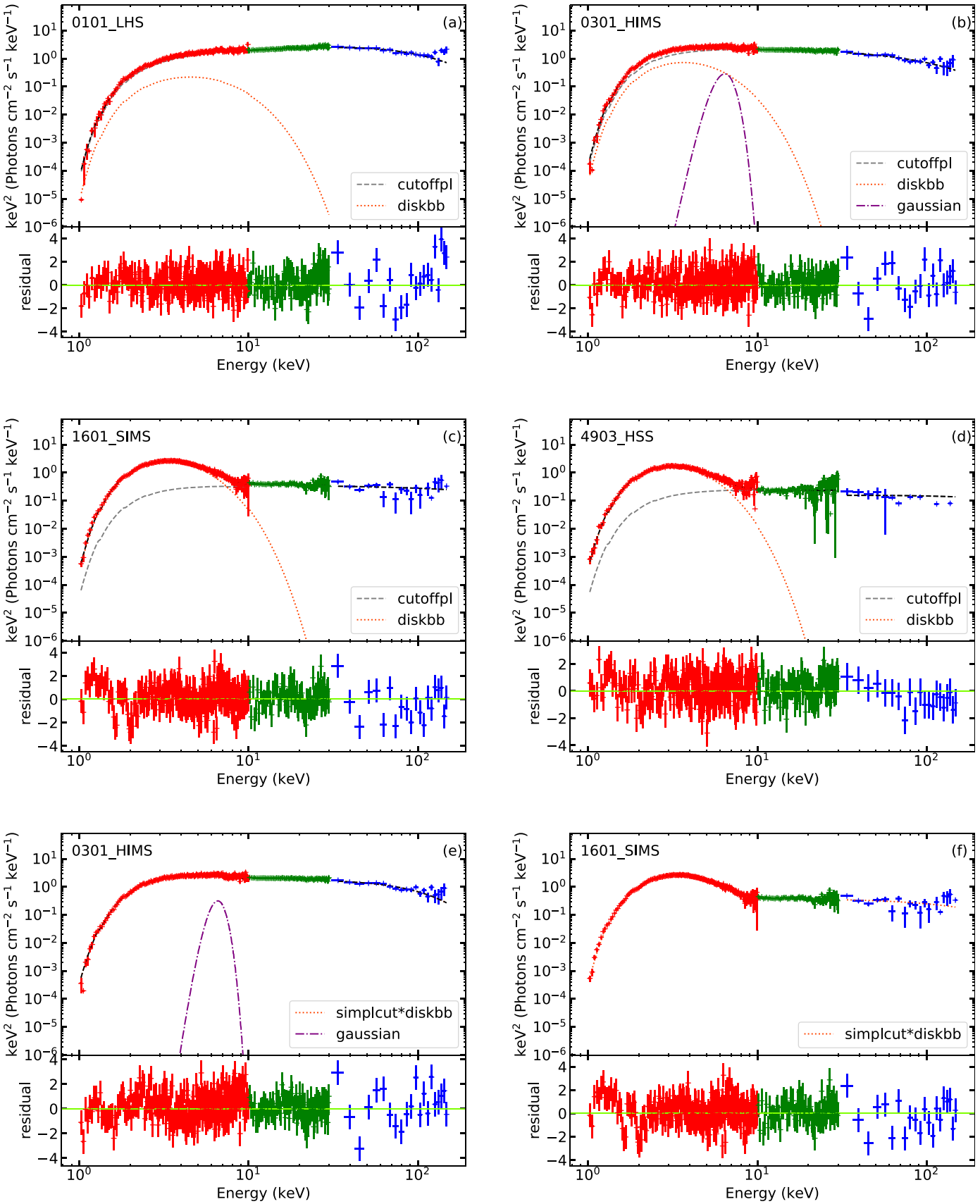

Figure 2. Unfolded spectra, model components, and fit residuals at different epochs (with the corresponding observation IDs labeled inside each panel). The red, green, and blue data points correspond to the LE, ME, and HE spectra, respectively.

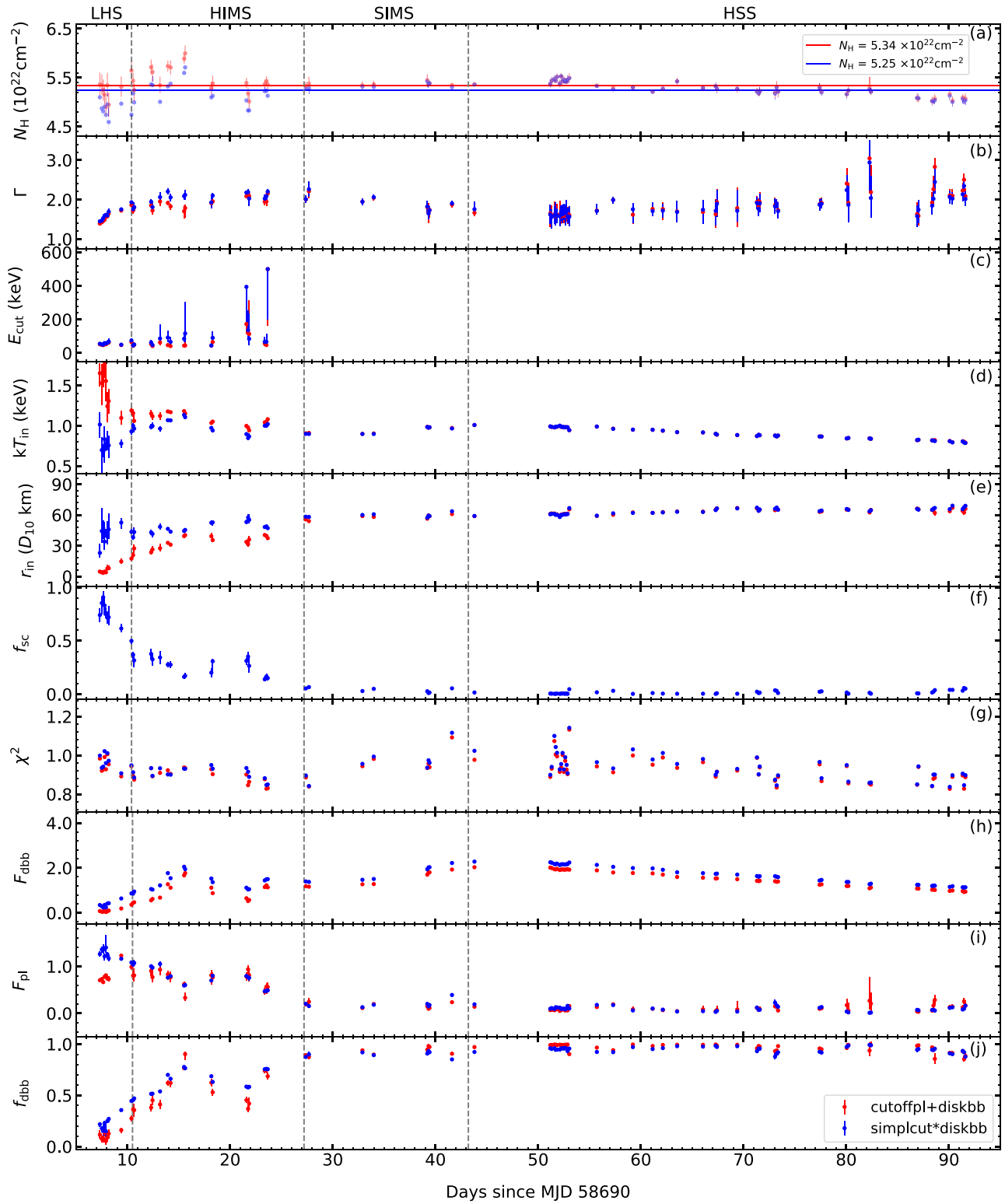

Figure 3. The best-fitting parameters of the Insight-HXMT spectra. The red and blue dots indicate the parameter values derived from the `cutoffpl+diskbb` and `simplcut*diskbb` models, respectively. Panel (a) shows the best-fitting values of the X-ray absorption column density, N_H, when it is left as a free parameter; it also shows the two constant values of N_H that we have adopted for further analysis, that is, $N_H = 5.34 \times 10^{22}$ cm^{-2} and $N_H = 5.25 \times 10^{22}$ cm^{-2} for `cutoffpl+diskbb` and `simplcut*diskbb`, respectively. The parameter values plotted in panels (b)–(j) are the best-fitting values for the models with fixed N_H. Γ is the photon index of the power-law or Comptonized component. E_{cut} is the exponential cutoff energy. This was unconstrained in the SIMS and HSS (no statistical improvement over a simple power law), and was fixed at 500 keV for fitting purposes in XSPEC; we omitted those values in panel (c). T_{in} is the peak color temperature of the disk. r_{in} is the apparent inner disk radius, defined as $r_{in} = \sqrt{N_{dbb}/\cos\theta} \times D_{10}$, where D_{10} is the source distance in units of 10 kpc and θ is the inclination angle of the accretion disk. We adopted $\theta = 73°$ (Draghis et al. 2020). f_{sc} is the scattered fraction, i.e., the proportion of disk photons scattered by the corona. F_{dbb} and F_{pl} stand for the unabsorbed bolometric flux of the disk component and the power-law component, respectively, in units of 10^{-8} erg cm^{-2} s^{-1}. f_{dbb} is the ratio between the disk flux and the total flux.

increase again in the SIMS and decrease slightly in the HSS. The power-law flux $F_{\rm pl}$ increased slowly in the LHS, then started to decrease after reaching the HIMS. The ratio between the disk flux and the total flux, $f_{\rm dbb}$, increased significantly in the LHS and HIMS, reached its peak in the SIMS, and remained almost constant ($\geqslant$90%) after that.

3.2.2. simplcut*diskbb Model

Before we try to attribute any physical meaning to the unusually small value of $r_{\rm in}$ in the LHS and HIMS, we need to be aware that a phenomenological cutoffpl+diskbb model does not self-consistently account for the photons that are removed from the disk component and upscattered into the power-law component. As a result, the normalization of the disk emission (hence, $r_{\rm in}$) is usually underestimated by such model when a corona is present (Yao et al. 2005). To get around this problem, we refitted the spectra with the self-consistent Comptonization model simplcut (Steiner et al. 2017) applied to a disk-blackbody seed spectrum.

When fitting the simplcutx*diskbb model, we adopted the same method as described in Section 3.2.1 to determine the value of $N_{\rm H}$. We fixed it at the mean value during the SIMS and HSS (5.25×10^{22} cm^{-2}; the blue line in Figure 3(a)) for all the subsequent spectral modeling.

Panels (e) and (f) of Figure 2 show two representative unfolded spectra and residuals based on the simplcut*−diskbb model (one for the HIMS and one for the SIMS).

The fitting statistics of the two models are equally good: the reduced χ^2 only varies by up to 2%. The best-fitting parameter values (Table 3) of the simplcut*diskbb model are shown as the blue dots in Figure 3. Compared to the cutoffpl model, the simplcut model has one more parameter: $f_{\rm sc}$, defined as the fraction of seed photons scattered into the power-law distribution. Its value decreases rapidly from ≈0.91 in the LHS to ≈0.13 in the HIMS, and then remains constant in the SIMS and HSS, at ≈0.05. As before, the high-energy cutoff is unconstrained for the observations in the SIMS and HSS. Most of the other parameters are consistent between the two models. In particular, we obtain the same best-fitting values of $r_{\rm in}$ and $T_{\rm in}$ for the SIMS and HSS observations. In the LHS and HIMS, however, the apparent radius derived from simplcut*−diskbb is higher than the value initially obtained from cutoffpl+diskbb, and the color temperature is lower. We argue that the self-consistent Comptonization model provides more plausible values of those two quantities. Although the anomalous behavior of $r_{\rm in}$ and $T_{\rm in}$ is now reduced, it is not entirely removed. Even in the Comptonization model, $r_{\rm in}$ is still smaller in the LHS and HIMS than in the HSS, and the disk temperature is surprisingly higher (≈1 keV) at those same epochs. This suggests that there is a physical reason for this strange behavior. We propose that it is caused by changes in the hardening factor.

3.3. Evolution of the Hardening Factor

The hardening factor (also called the color-correction factor) $f_{\rm col}$ accounts for the deviation of the disk emission from a pure blackbody spectrum (Shimura & Takahara 1995). The peak effective temperature $T_{\rm eff}$ is related to the fitted color temperature $T_{\rm in}$ by the relation $T_{\rm eff} = T_{\rm in}/f_{\rm col}$. Conversely, the relation between the physical inner radius, $R_{\rm in}$, and the apparent inner radius, $r_{\rm in}$, is:

$$R_{\rm in} = r_{\rm in}\, \xi\, f_{\rm col}^2 = \sqrt{N_{\rm dbb}/\cos\theta}\, \xi\, f_{\rm col}^2\, D_{10}, \quad (1)$$

(Kubota et al. 1998), where $\xi = 0.412$ is the general relativity correction factor, $N_{\rm dbb}$ is the diskbb normalization, θ is the inclination angle of the accretion disk, and D_{10} is the distance in units of 10 kpc. We can plausibly assume that $R_{\rm in} \approx R_{\rm ISCO}$ and $f_{\rm col} \approx 1.7$ (the "canonical" value from Shimura & Takahara 1995) in the SIMS and at least near the peak of the HSS, before the start of the decline (i.e., MJD 58717–58745). We adopt an inclination angle of 73° (Draghis et al. 2020). The distance is completely unconstrained, in the absence of a detected optical counterpart.[13] The fitted value of $r_{\rm in}$ at the first epoch of the HSS is 59.0 ± 0.5 D_{10} km, and indeed this value remains substantially unchanged throughout MJD 58717–58745. Then, from Equation (1), $R_{\rm ISCO} = 70.3 \pm 0.6\, D_{10}$ km. In the LHS and HIMS, the physical inner radius $R_{\rm in}$ must be at least as large as $R_{\rm ISCO}$ (it may be equal, if there is already a condensed thin disk in the innermost region). Thus, in our proposed scenario, we can determine the minimum value of $f_{\rm col}$ required to make $R_{\rm in} \geqslant R_{\rm ISCO}$ at the early epochs. We obtain $f_{\rm col} \gtrsim 2.7$ in the first few days of the LHS observations. In the latter parts of the LHS and HIMS, $f_{\rm col}$ decreases to ≈1.7–2.4. Conversely, in the declining phase of the HSS, a canonical value $f_{\rm col} = 1.7$ implies $R_{\rm in} \geqslant R_{\rm ISCO}$. This can be interpreted in two alternative ways: either the inner disk was starting to recede from the ISCO after MJD 58745, or it was still at the ISCO, but the hardening factor declined to $f_{\rm col} \approx 1.6$. Finally, we derive the effective temperature $T_{\rm eff} = T_{\rm in}/f_{\rm col}$. We find that with our estimated hardening factors, $T_{\rm eff}$ increased monotonically during the LHS (as expected), instead of showing an unphysical decline in the first part of the outburst. We show the evolution of the radii, temperatures, and $f_{\rm col}$ in Figure 4.

4. Discussion

4.1. The Inner Disk Radius in the Initial Hard State

The early stages of transient BH outbursts are characterized by the coupled evolution of a corona and the underlying disk. For EXO 1846−031, the evolution of the coronal parameters follows the canonical expectations. For example, the scattering fraction $f_{\rm sc}$ follows the same trend as seen in recent outbursts of well-known BH transients such as GX 339–4 (Sridhar et al. 2020), XTE J1550564 (Connors et al. 2020), and 4U 1630–47 (Connors et al. 2021). The evolution of the disk parameters may have subtle differences.

Our spectral modeling shows (Section 3.2) that if the hardening factor $f_{\rm col}$ is kept constant from the LHS to the HSS, the inner radius of the disk is smaller in the LHS than in the HSS. We reject this possibility as unphysical: the inner disk radius in the LHS must be at least as large as in the HSS. If we assume that the inner disk radius is constant throughout the entire outburst, $f_{\rm col}$ must be decreasing from ≈2.7 at the beginning of the outburst, toward the canonical value of ≈1.6 in the HSS. With this assumption, we preserve the scaling law $F_{\rm dbb} \propto T_{\rm eff}^4$ throughout the outburst, characteristic of a radiatively efficient disk with constant inner radius. Finally, if we also allow for the possibility that $R_{\rm in} > R_{\rm ISCO}$ in the LHS,

[13] The value of 7 kpc introduced by Parmar et al. (1993) is only a guess, based on a now-out-of-date analogy with the luminosity of other BH transients.

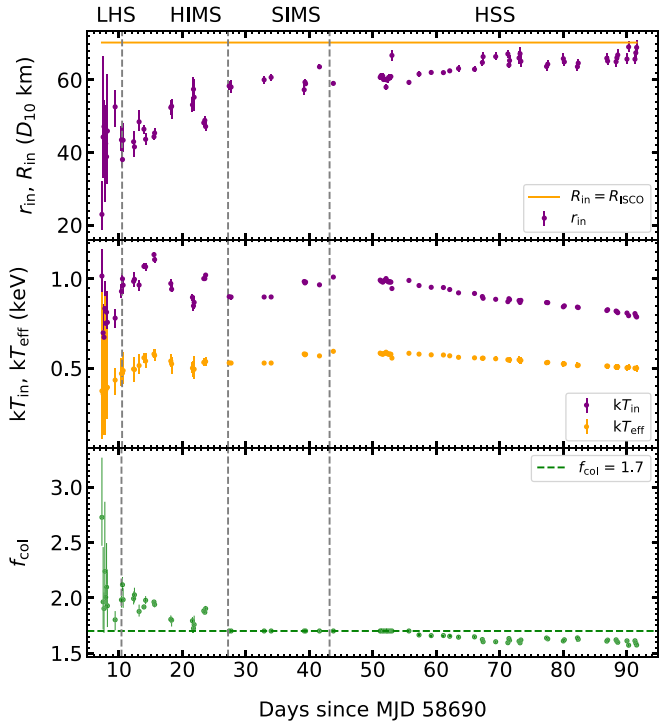

Figure 4. The evolutions of $T_{\rm eff}$, $R_{\rm in}$, and $f_{\rm col}$. $f_{\rm col}$ is calculated from $R_{\rm in} = r_{\rm in}\,\xi\,f_{\rm col}^2$ under the assumption that $R_{\rm in} = R_{\rm ISCO}$. Then, $T_{\rm eff}$ is calculated from $T_{\rm eff} = T_{\rm in}/f_{\rm col}$. The purple dots represent $T_{\rm in}$ and $r_{\rm in}$ obtained from the `simplcut*diskbb` model, while the orange dots and the orange line indicate $T_{\rm eff}$ and $R_{\rm in} = R_{\rm ISCO}$, respectively. If $R_{\rm in} > R_{\rm ISCO}$ in the LHS and HIMS, the values of $T_{\rm eff}$ plotted in the middle panel are the upper limits of the true effective temperature, and the values of $f_{\rm col}$ in the bottom panel are the lower limits of the hardening factor.

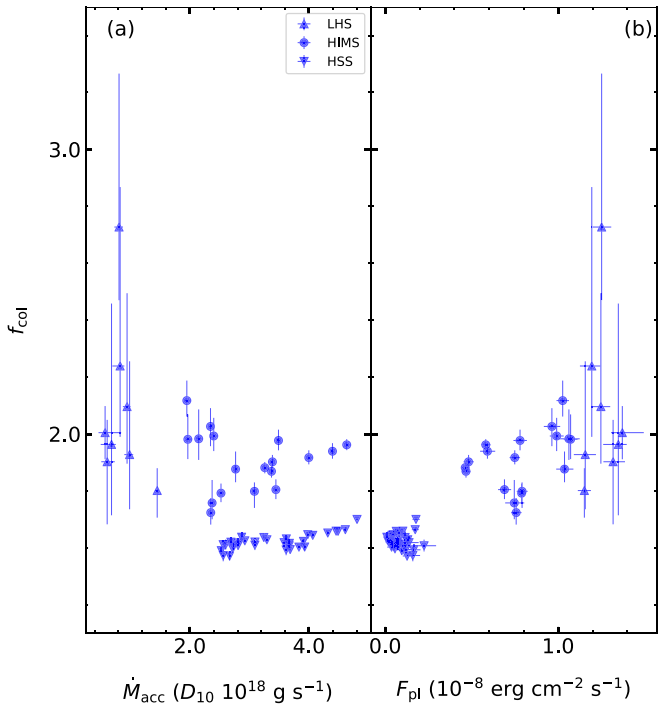

Figure 5. $f_{\rm col}$ as a function of the mass accretion rate $\dot{M}_{\rm acc}$ (a) and the power-law flux $F_{\rm pl}$ (b), respectively. The mass accretion rate is roughly estimated as $\dot{M}_{\rm acc} = L/(\eta c^2)$, where the efficiency $\eta = 0.1$ is assumed. The blue upward triangles, circles, and downward triangles represent the LHS, HIMS, and HSS, respectively.

the hardening factor must be even higher at the beginning of the outburst ($f_{\rm col} > 2.7$).

In previous studies of BH transients, a canonical value of $f_{\rm col} \approx 1.7$ (from Shimura & Takahara 1995) has usually been adopted for the soft state, to account for a "diluted" disk spectrum. However, there are several observations of BH outbursts that show convincing evidence of a variable hardening factor, especially in the initial hard state. For example, in GX 339–4, Salvesen et al. (2013) proposed that a variable hardening factor is an alternative to disk truncation, to explain the changes in the disk spectrum. Other sources with possible evidence of a variable hardening factor are 4U 1957+11 (Maitra et al. 2014), MAXI J1820+070 (Guan et al. 2021), and MAXI J1348−630 (Zhang et al. 2022). From simulations of disk spectra, Merloni et al. (2000) also suggested a variable hardening factor $f_{\rm col} \approx 1.7$–3, arguing that $f_{\rm col}$ increases when the disk emission is relatively less dominant. This result is supported by a global study of disk properties by Dunn et al. (2011). They found that for almost all BH transients, $f_{\rm col}$ is relatively stable in the disk-dominated state, but increases from 1.6 to 2.6 as the disk fraction decreases. The variation in $f_{\rm col}$ may be caused by changes in the accretion energy dissipation (Merloni et al. 2000), in the vertical disk structure (Davis et al. 2005), in the magnetic energy density (Blaes et al. 2006), and in the disk density and optical depth (Soria et al. 2008).

The presence or absence of a full disk also has important implications for the interpretation of QPOs. LFQPOs with a centroid frequency between 0.7 and 8 Hz have been detected in the HIMS of EXO 1846–031 by Liu et al. (2021), from a timing analysis of the same Insight-HXMT data used in this work. If there was already a thin disk at or very close to the ISCO, as we have suggested here, this geometry disfavors QPO models (e.g., Stella & Vietri 1998; Ingram et al. 2009; Varniere & Vincent 2016) that require significant changes in the inner disk edge. Instead, jet precession would be a viable model. The presence of a jet in EXO 1846−031 was confirmed by VLA (Miller-Jones et al. 2019) and MeerKAT (Williams et al. 2019) detections in the HIMS. By comparison, the BH transient MAXI J1820+070 is another source for which LFQPOs have been detected in the LHS (e.g., Wang et al. 2020; Ma et al. 2021), and the disk is thought to be nontruncated based on the reflection-fitting method (Buisson et al. 2019). A likely interpretation for the origin of the QPOs is jet precession (Ma et al. 2021).

4.2. Additional Contributions to the Hardening Factor in the LHS and HIMS

Done & Davis (2008) reported a detailed investigation of $f_{\rm col}$ in a disk-dominated state. Their work shows that $f_{\rm col}$ increases as the mass accretion rate $\dot{M}_{\rm acc}$ increases, which links the variation of $f_{\rm col}$ to the mass accretion rate. To examine whether this relationship is still valid in a hard state, we plot $f_{\rm col}$ as a function of $\dot{M}_{\rm acc}$ in the LHS, the HIMS, and most of the HSS in Figure 5(a). Data points between MJD 58717 and 58745 are excluded here, since we have assumed a constant $f_{\rm col}$ in this period (as explained in Section 3.3). It is clear that $f_{\rm col}$ and $\dot{M}_{\rm acc}$ indeed show a positive correlation in the HSS, which is in good agreement with the results of Done & Davis (2008). However, the values of $f_{\rm col}$ in the LHS and HIMS, where $\dot{M}_{\rm acc}$ are relatively low, are significantly higher than that in the HSS. We

thus suspect that there should be additional contributions to the $f_{\rm col}$ in the LHS and HIMS.

We show the relationship between $f_{\rm col}$ and the power-law flux $F_{\rm pl}$ in Figure 5(b), in which $f_{\rm col}$ increases as $F_{\rm pl}$ increases throughout the outburst. Apparently, $F_{\rm pl}$ gradually decreases as the source evolves from the LHS to the HIMS, and becomes negligible in the HSS. This implies that the high value of $f_{\rm col}$ in the LHS and the HIMS is probably associated with the hard emission. Compared to the HSS, the additional power-law emission in the hard state will heat up the disk surface, leading to an increase in the disk temperature, which results in a significant increase in $f_{\rm col}$. Similar results of $f_{\rm col}$ increasing as the disk fraction decreases have been reported by Merloni et al. (2000) and Dunn et al. (2011). We plot $f_{\rm col}$ versus $F_{\rm pl}$ in Figure 5(b), which emphasizes the contribution of the power-law flux when the source is in the LHS and HIMS.

4.3. Constraints on System Parameters

Using the reflection-fitting method, Draghis et al. (2020) obtained a spin parameter as high as $a_* = 0.997^{+0.001}_{-0.002}$. They applied 12 reflection models to the NuSTAR spectra to test this value, with different assumptions of the coronal geometry, disk density, and emission spectrum, and obtained consistent spin values. However, Wang et al. (2021) studied the same NuSTAR data with two reflection models and argued that the spin cannot be constrained. Here, we try to constrain the spin parameter with the continuum-fitting method, and test whether the result is consistent with the extreme value claimed by Draghis et al. (2020).

As discussed in Section 3.3, the inner disk radius reached the ISCO in the HSS, with $R_{\rm ISCO} \approx 70\, D_{10}$ km (for $f_{\rm col} = 1.7$ and $\theta = 73°$). We apply the relationship between the ISCO radius and the spin parameter (Zhang et al. 1997a; see also Bardeen et al. 1972):

$$R_{\rm ISCO} = \begin{cases} (3 + A_2 + \sqrt{(3 - A_1)(3 + A_1 + 2A_2)}) \times r_{\rm g}, & a_* \leqslant 0 \\ (3 + A_2 - \sqrt{(3 - A_1)(3 + A_1 + 2A_2)}) \times r_{\rm g}, & a_* > 0, \end{cases} \quad (2)$$

where $r_{\rm g} = GM_{\rm BH}/c^2$, $A_1 = 1 + (1 - a_*^2)^{1/3}[(1 + a_*)^{1/3} + (1 - a_*)^{1/3}]$, and $A_2 = (3a_*^2 + A_1^2)^{1/2}$. Thus, from Equation (2), we can derive a_* as a function of $M_{\rm BH}$ and distance. Since neither the BH mass nor the distance is known, we determine a_* over a grid of values spanning a mass range of 5–15 $M_\odot$ (based on the distribution of kinematic masses in Galactic BH transients; Özel et al. 2010; Corral-Santana et al. 2016) and a distance D of 2–12 kpc (based on the distribution of Galactic BH distances in Tetarenko et al. 2016).

The values of the spin parameter versus BH mass for different distances are shown in Figure 6(a). The extreme value of $a_* \approx 0.997$ suggested by Draghis et al. (2020) is consistent only with a small distance ($D \approx 2$–4 kpc) and a relatively high mass ($M_{\rm BH} > 7M_\odot$). However, this combination of mass and distance would imply a peak Eddington ratio $\lambda \equiv L_{\rm disk}/L_{\rm Edd} \approx 0.02$–$0.04$ in the HSS. This is much lower than the typical X-ray luminosities observed in the disk-dominated states of other Galactic BHs (Tetarenko et al. 2016). We also calculate the spin parameter when the inclination is assumed to be 40° (Wang et al. 2021), as shown in Figure 6(b). In this case, the extreme value of $a_* \approx 0.997$ is consistent with the combination of distance ($D \approx 2$–6 kpc) and mass

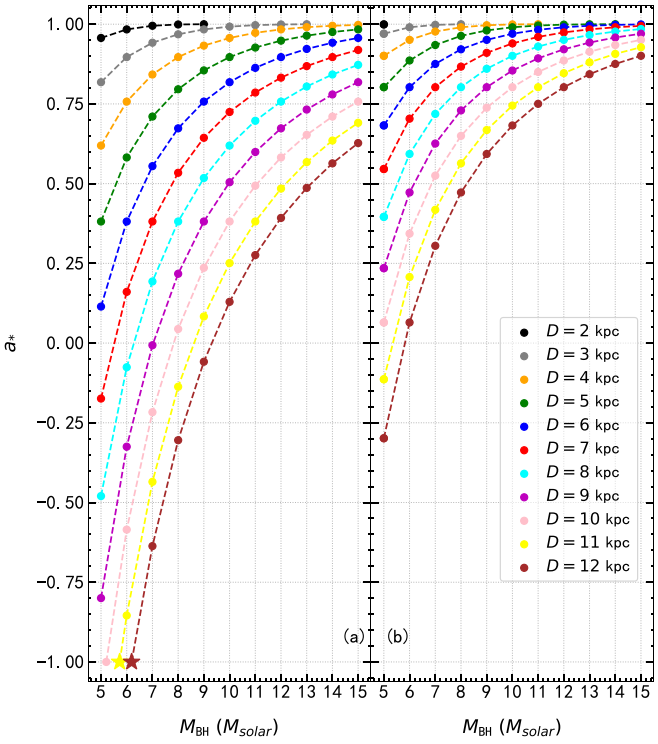

Figure 6. Spin parameter as a function of BH mass and distance to EXO 1846–031, when the inclination is assumed to be 73° (a) or 40° (b). The stars mark the lowest acceptable limit of the BH mass for a given distance.

($M_{\rm BH} \approx 5$–$14\ M_\odot$). The corresponding peak Eddington ratio would then be ≈ 0.1, but this is still lower than expected and observed in most other systems (Tang et al. 2011; Yan & Yu 2015). For a higher Eddington ratio, the spin parameter has to be nonextremal.

Previous work has already reported the inconsistency of the spin measurements obtained for the same systems using the reflection-fitting and continuum-fitting methods. For example, for GRO J1655−40, the reflection-fitting method provides a higher spin than the continuum-fitting method (Shafee et al. 2006; Reis et al. 2009; Reynolds 2014), similar to what we have found here for EXO 1846−031. Allowing for the uncertainties in $f_{\rm col}$ at a level of ± 0.2–0.3 can alleviate the discrepancy (Salvesen & Miller 2021); this effect is more pronounced for nonextremal spins. For example, if we assume a smaller value of the hardening factor, $f_{\rm col} = 1.4$, we can reach $a_* = 0.997$ for $D \approx 5$–6 kpc and $M_{\rm BH} \gtrsim 12M_\odot$ at $\theta = 73°$, or $D \approx 4$–9 kpc and $M_{\rm BH} \approx 6$–$14\ M_\odot$ at $\theta = 40°$. The corresponding peak Eddington ratios would then be ≈ 0.09 and ≈ 0.22, respectively.

In general, for the same continuum parameters, lower values of $f_{\rm col}$ imply higher Eddington ratios. We conclude that, in principle, the inconsistency of the spin parameter measured using the continuum-fitting and reflection-fitting methods can be somewhat mitigated by the choice of $f_{\rm col}$. However, without knowing its mass and distance, we cannot draw a further conclusion about the spin parameter of the BH in EXO 1846–031.

5. Conclusions

We have presented a broadband (1–150 keV band) spectral analysis of the 2019 outburst of the BH candidate EXO 1846−031, based on Insight-HXMT observations. The

source exhibited state transitions from the LHS to the HIMS, the SIMS, and the HSS. The broadband spectra can be well modeled with `diskbb` plus `cutoffpl` components. Most of the best-fitting parameter values are consistent with those inferred in other "canonical" BH transients. In particular, the almost constant `diskbb` normalization in the SIMS and HSS indicates that the accretion disk reached the ISCO in the two states, suggesting a value of $R_{\rm ISCO} \approx 70\, D_{10}$ km. However, the apparent inner radius in the LHS and HIMS is unphysically small (at some epochs, smaller than that in the HSS), even after we take into account the fraction of disk photons upscattered into the Comptonization component. In order to ensure that the true radius is at least never smaller than the ISCO in the hard state, we need to allow for a variable hardening factor, decreasing as the outburst progresses and the disk becomes brighter and more dominant. If we normalize the hardening factor to its canonical value $f_{\rm col} = 1.7$ at the SIMS and the beginning of the HSS, we find that $f_{\rm col} \gtrsim 2.7$ at the beginning of the LHS. Conversely, the last phase of the HSS is consistent with a small decrease in $f_{\rm col}$ below the canonical value.

Furthermore, we find that the value of the hardening factor in the relatively hard states is significantly higher than that in the HSS. We suggest that coronal irradiation onto the disk provides additional contributions to the hardening factor in the LHS and HIMS.

Using our continuum-fitting parameters, we also tested previous claims of extreme spin for this BH, inferred from reflection-fitting. We derived the range of acceptable spin values as a function of a plausible range of BH masses and distances, based on two inclination angles. The inconsistency of the spin measured with the continuum-fitting and reflection-fitting methods is partly due to the different choices of $f_{\rm col}$.

In conclusion, our study has shown that $f_{\rm col}$ plays an important role in the intrinsic emission and physical parameters of the accretion disk, and in our understanding of the outburst evolution. It also influences the measurement of the spin parameter in the continuum-fitting method. Therefore, we argue that $f_{\rm col}$ should never simply be assumed as a constant value, especially when the disk emission evolves over a broad range of luminosities (Salvesen et al. 2013). More specifically, in the case of EXO 1846−031, there is empirical evidence that the accretion disk was already close to the ISCO in the initial hard state (unless $f_{\rm col} \gtrsim 2.7$). A similar noncanonical interpretation has been proposed for several other transient BH candidates (Reis et al. 2008, 2010; Parker et al. 2015; García et al. 2018, 2019; Buisson et al. 2019; Kara et al. 2019). Simultaneous broadband investigations of the early outburst evolution in BH X-ray binaries, such as those made possible by Insight-HXMT, hold the key to the physical understanding of state transitions.

This work has made use of data from the Insight-HXMT mission, a project funded by the China National Space Administration (CNSA) and the Chinese Academy of Sciences (CAS). This work is supported by the National Key R&D Program of China (2021YFA0718500) and the National Natural Science Foundation of China under grants U1838201, 11473027, U1838202, 11733009, U1838104, U1938101, U1838115, U2038101, and U1938103, and NSF grant 12073029. Y.W. acknowledges support from the Royal Society Newton Funds. J.L. thanks the Guangdong Major Project of Basic and Applied Basic Research (grant No. 2019B030302001). R.S. is grateful for NSF grant 12073029.

Facility: Insight-HXMT.

ORCID iDs

X. Q. Ren https://orcid.org/0000-0002-0765-5101
S. N. Zhang https://orcid.org/0000-0001-5586-1017
R. Soria https://orcid.org/0000-0002-4622-796X
L. Tao https://orcid.org/0000-0002-2705-4338
J. L. Qu https://orcid.org/0000-0002-9796-2585
L. M. Song https://orcid.org/0000-0003-0274-3396
M. Y. Ge https://orcid.org/0000-0002-2749-6638
J. Y. Liao https://orcid.org/0000-0001-8277-6133
R. C. Ma https://orcid.org/0000-0003-3260-8718
Y. L. Tuo https://orcid.org/0000-0003-3127-0110
D. K. Zhou https://orcid.org/0000-0002-7420-9988

References

Aneesha, U., Mandal, S., & Sreehari, H. 2019, MNRAS, 486, 2705
Arnaud, K. A. 1996, in ASP Conf. Ser. 101, Astronomical Data Analysis Software and Systems V, ed. G. H. Jacoby & J. Barnes (San Francisco, CA: ASP), 17
Bardeen, J. M., Press, W. H., & Teukolsky, S. A. 1972, ApJ, 178, 347
Barrière, N. M., Krivonos, R., Tomsick, J. A., et al. 2015, ApJ, 799, 123
Belloni, T., Homan, J., Casella, P., et al. 2005, A&A, 440, 207
Belloni, T. M. 2010, in States and Transitions in Black Hole Binaries, ed. T. Belloni, Vol. 794 (Berlin: Springer), 53
Belloni, T. M., & Motta, S. E. 2016, in Transient Black Hole Binaries, ed. C. Bambi, Vol. 440 (Berlin: Springer), 61
Belloni, T. M., & Stella, L. 2014, SSRv, 183, 43
Bhalerao, V., Romano, P., Tomsick, J., et al. 2015, MNRAS, 447, 2274
Blackburn, J. K. 1995, in ASP Conf. Ser. 77, Astronomical Data Analysis Software and Systems IV, ed. R. A. Shaw, H. E. Payne, & J. J. E. Hayes (San Francisco, CA: ASP), 367
Blaes, O. M., Davis, S. W., Hirose, S., Krolik, J. H., & Stone, J. M. 2006, ApJ, 645, 1402
Buisson, D. J. K., Fabian, A. C., Barret, D., et al. 2019, MNRAS, 490, 1350
Bult, P. M., Gendreau, K. C., Arzoumanian, Z., et al. 2019, ATel, 12976, 1
Cao, X., Jiang, W., Meng, B., et al. 2020, SCPMA, 63, 249504
Chen, W., Shrader, C. R., & Livio, M. 1997, ApJ, 491, 312
Chen, Y., Cui, W., Li, W., et al. 2020, SCPMA, 63, 249505
Connors, R. M. T., García, J. A., Dauser, T., et al. 2020, ApJ, 892, 47
Connors, R. M. T., García, J. A., Tomsick, J., et al. 2021, ApJ, 909, 146
Corral-Santana, J. M., Casares, J., Muñoz-Darias, T., et al. 2016, A&A, 587, A61
Dauser, T., Garcia, J., Wilms, J., et al. 2013, MNRAS, 430, 1694
Davis, S. W., Blaes, O. M., Hubeny, I., & Turner, N. J. 2005, ApJ, 621, 372
Davis, S. W., & El-Abd, S. 2019, ApJ, 874, 23
Done, C., & Davis, S. W. 2008, ApJ, 683, 389
Done, C., Gierliński, M., & Kubota, A. 2007, A&ARv, 15, 1
Draghis, P. A., Miller, J. M., Cackett, E. M., et al. 2020, ApJ, 900, 78
Dunn, R. J. H., Fender, R. P., Körding, E. G., Belloni, T., & Merloni, A. 2011, MNRAS, 411, 337
Eardley, D. M., Lightman, A. P., & Shapiro, S. L. 1975, ApJL, 199, L153
Esin, A. A., McClintock, J. E., & Narayan, R. 1997, ApJ, 489, 865
Fabian, A. C., Rees, M. J., Stella, L., & White, N. E. 1989, MNRAS, 238, 729
Fender, R. P., Belloni, T. M., & Gallo, E. 2004, MNRAS, 355, 1105
García, J., Dauser, T., Lohfink, A., et al. 2014, ApJ, 782, 76
García, J. A., Steiner, J. F., Grinberg, V., et al. 2018, ApJ, 864, 25
García, J. A., Tomsick, J. A., Sridhar, N., et al. 2019, ApJ, 885, 48
Ge, M. Y., Ji, L., Zhang, S. N., et al. 2020, ApJL, 899, L19
Guan, J., Tao, L., Qu, J. L., et al. 2021, MNRAS, 504, 2168
Guo, C.-C., Liao, J.-Y., Zhang, S., et al. 2020, JHEAp, 27, 44
Homan, J., & Belloni, T. 2005, Ap&SS, 300, 107
Homan, J., Wijnands, R., van der Klis, M., et al. 2001, ApJS, 132, 377
Ingram, A., Done, C., & Fragile, P. C. 2009, MNRAS, 397, L101
Kara, E., Steiner, J. F., Fabian, A. C., et al. 2019, Natur, 565, 198
Kubota, A., Tanaka, Y., Makishima, K., et al. 1998, PASJ, 50, 667
Li, X., Li, X., Tan, Y., et al. 2020, JHEAp, 27, 64
Liao, J.-Y., Zhang, S., Chen, Y., et al. 2020a, JHEAp, 27, 24
Liao, J.-Y., Zhang, S., Lu, X.-F., et al. 2020b, JHEAp, 27, 14

Liu, B. F., Taam, R. E., Meyer-Hofmeister, E., & Meyer, F. 2007, ApJ, 671, 695
Liu, C., Zhang, Y., Li, X., et al. 2020, SCPMA, 63, 249503
Liu, H.-X., Huang, Y., Xiao, G.-C., et al. 2021, RAA, 21, 070
Ma, X., Tao, L., Zhang, S.-N., et al. 2021, NatAs, 5, 94
Maitra, D., Miller, J. M., Reynolds, M. T., Reis, R., & Nowak, M. 2014, ApJ, 794, 85
Makishima, K., Maejima, Y., Mitsuda, K., et al. 1986, ApJ, 308, 635
McClintock, J. E., Narayan, R., & Steiner, J. F. 2014, SSRv, 183, 295
Mereminskiy, I. A., Krivonos, R. A., Medvedev, P. S., & Grebenev, S. A. 2019, ATel, 12969, 1
Merloni, A., Fabian, A. C., & Ross, R. R. 2000, MNRAS, 313, 193
Miller, J. M., Homan, J., & Miniutti, G. 2006, ApJL, 652, L113
Miller, J. M., Reynolds, C. S., Fabian, A. C., Miniutti, G., & Gallo, L. C. 2009, ApJ, 697, 900
Miller, J. M., Zoghbi, A., Gandhi, P., & Paice, J. 2019, ATel, 13012, 1
Miller-Jones, J., Russell, T., Sivakoff, G., & Tetarenko, A. 2019, ATel, 12977, 1
Mitsuda, K., Inoue, H., Koyama, K., et al. 1984, PASJ, 36, 741
Motta, S., Homan, J., Muñoz Darias, T., et al. 2012, MNRAS, 427, 595
Motta, S. E. 2016, AN, 337, 398
Muñoz-Darias, T., Motta, S., Stiele, H., & Belloni, T. M. 2011, MNRAS, 415, 292
Narayan, R., & Yi, I. 1995, ApJ, 452, 710
Negoro, H., Nakajima, M., Sugita, S., et al. 2019, ATel, 12968, 1
Özel, F., Psaltis, D., Narayan, R., & McClintock, J. E. 2010, ApJ, 725, 1918
Parker, M. L., Tomsick, J. A., Miller, J. M., et al. 2015, ApJ, 808, 9
Parmar, A. N., Angelini, L., Roche, P., & White, N. E. 1993, A&A, 279, 179
Peris, C. S., Remillard, R. A., Steiner, J. F., et al. 2016, ApJ, 822, 60
Plotkin, R. M., Gallo, E., Markoff, S., et al. 2015, MNRAS, 446, 4098
Reis, R. C., Fabian, A. C., & Miller, J. M. 2010, MNRAS, 402, 836
Reis, R. C., Fabian, A. C., Ross, R. R., & Miller, J. M. 2009, MNRAS, 395, 1257
Reis, R. C., Fabian, A. C., Ross, R. R., et al. 2008, MNRAS, 387, 1489
Remillard, R. A., & McClintock, J. E. 2006, ARA&A, 44, 49
Reynolds, C. S. 2014, SSRv, 183, 277
Reynolds, M. T., & Miller, J. M. 2013, ApJ, 769, 16
Salvesen, G., & Miller, J. M. 2021, MNRAS, 500, 3640
Salvesen, G., Miller, J. M., Reis, R. C., & Begelman, M. C. 2013, MNRAS, 431, 3510
Shafee, R., McClintock, J. E., Narayan, R., et al. 2006, ApJL, 636, L113
Shimura, T., & Takahara, F. 1995, ApJ, 445, 780
Sidoli, L., Tiengo, A., Paizis, A., et al. 2017, ApJ, 838, 133
Soria, R., Wu, K., & Kunic, Z. 2008, in Proc. of ESAC Faculty Workshop on X-rays from Nearby Galaxies, ed. S. Carpano, M. Ehle, & W. Pietsch (Munich: Max-Planck-Institut), 48
Sridhar, N., García, J. A., Steiner, J. F., et al. 2020, ApJ, 890, 53
Steiner, J. F., García, J. A., Eikmann, W., et al. 2017, ApJ, 836, 119
Steiner, J. F., Narayan, R., McClintock, J. E., & Ebisawa, K. 2009, PASP, 121, 1279
Steiner, J. F., Reis, R. C., McClintock, J. E., et al. 2011, MNRAS, 416, 941
Stella, L., & Vietri, M. 1998, ApJL, 492, L59
Sunyaev, R. A., & Titarchuk, L. G. 1980, A&A, 500, 167
Tanaka, Y., & Shibazaki, N. 1996, ARA&A, 34, 607
Tang, J., Yu, W.-F., & Yan, Z. 2011, RAA, 11, 434
Tao, L., Tomsick, J. A., Walton, D. J., et al. 2015, ApJ, 811, 51
Tao, L., Chen, Y., Güngör, C., et al. 2018, MNRAS, 480, 4443
Tetarenko, B. E., Sivakoff, G. R., Heinke, C. O., & Gladstone, J. C. 2016, ApJS, 222, 15
Tomsick, J. A., & Kaaret, P. 2000, ApJ, 537, 448
van der Klis, M. 2006, in Compact Stellar X-ray Sources, ed. W. Lewin & M. van der Kils, Vol. 39 (Cambridge: Cambridge Univ. Press)
Varniere, P., & Vincent, F. H. 2016, A&A, 591, A36
Wang, Y., Ji, L., Zhang, S. N., et al. 2020, ApJ, 896, 33
Wang, Y., Ji, L., García, J. A., et al. 2021, ApJ, 906, 11
Williams, D., Fender, R., Woudt, P., & Miller-Jones, J. 2019, ATel, 12992, 1
Wilms, J., Allen, A., & McCray, R. 2000, ApJ, 542, 914
Yan, Z., & Yu, W. 2015, ApJ, 805, 87
Yang, Y.-J., Soria, R., Russell, D., et al. 2019a, ATel, 13036, 1
Yang, Y.-J., Xiao, G., Soria, R., et al. 2019b, ATel, 13037, 1
Yao, Y., Zhang, S. N., Zhang, X., Feng, Y., & Robinson, C. R. 2005, ApJ, 619, 446
Zdziarski, A. A., De Marco, B., Szanecki, M., Niedźwiecki, A., & Markowitz, A. 2021, ApJ, 906, 69
Zhang, L., Altamirano, D., Cúneo, V. A., et al. 2020a, MNRAS, 499, 851
Zhang, S., Lu, F. J., Zhang, S. N., & Li, T. P. 2014, Proc. SPIE, 9144, 914421
Zhang, S. N., Cui, W., & Chen, W. 1997a, ApJL, 482, L155
Zhang, S. N., Ebisawa, K., Sunyaev, R., et al. 1997b, ApJ, 479, 381
Zhang, S.-N., Li, T., Lu, F., et al. 2020b, SCPMA, 63, 249502
Zhang, W., Tao, L., Soria, R., et al. 2022, ApJ, 927, 210